Master's thesis

NTNU
Norwegian University of Science and Technology
Faculty of Natural Sciences
Department of Chemical Engineering

Anette Synnøve Groven

Conversion of Biomass-derived Synthesis Gas via the Fischer-Tropsch Synthesis using Cobalt-based Catalysts

Master's thesis in Chemical Engineering and Biotechnology
Supervisor: Edd Anders Blekkan
Co-supervisor: Oscar Luis Ivanez Encinas, Kumar Ranjan Rout
June 2022

NTNU
Norwegian University of
Science and Technology

Anette Synnøve Groven

Conversion of Biomass-derived Synthesis Gas via the Fischer-Tropsch Synthesis using Cobalt-based Catalysts

Master's thesis in Chemical Engineering and Biotechnology
Supervisor: Edd Anders Blekkan
Co-supervisor: Oscar Luis Ivanez Encinas, Kumar Ranjan Rout
June 2022

Norwegian University of Science and Technology
Faculty of Natural Sciences
Department of Chemical Engineering

NTNU
Norwegian University of
Science and Technology

Preface

This thesis is a fulfilment of the course TKP4901-"Chemical Process Technology, Master's Thesis", and was written for the Catalysis Group in the Department of Chemical Engineering at the Norwegian University of Science and Technology (NTNU).

I want to express my gratitude to Edd A. Blekkan, my supervisor, for his expert guidance and impressive knowledge in this field. I would also like to thank my co-supervisor Kumar R. Rout. I especially want to thank Oscar Luis Ivanez Encinas, co-supervisor and Ph.D candidate, for his invaluable assistance and mentoring throughout this project.

Finally, I want to thank all of my wonderful friends for making my five years in Trondheim so enjoyable and memorable. And last but not least, I want to thank my family for their unwavering support and encouragement during my education.

Declaration of Compliance

I, Anette Synnøve Groven, declare that this is an independent work according to the exam regulations of the Norwegian University of Science and Technology.

Trondheim, Norway 13.06.2022

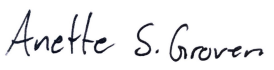

Anette Synnøve Groven

Abstract

The current global energy scenario, as well as the threat of environmental destruction, encourages the use of renewable energy resources to replace fossil fuels. Biomass is one of the most promising carbon-neutral renewable resource for the sustainable production of biofuels and important chemicals. Biofuels can be made through a sequence of processes in which biomass is first gasified into synthesis gas and then converted into liquid fuels via the catalyzed Fischer-Tropsch process. The synthesis gas made from biomass contains a series of impurities that can cause complications for the sensitive Fischer-Tropsch catalyst. The Fischer-Tropsch synthesis produces a wide range of hydrocarbons, one of which is light olefins, the most essential chemical intermediate for multiple industries.

In this study, the effect of support material, manganese promotion, and phosphorous contamination on cobalt-based Fischer-Tropsch catalysts were investigated. Phosphorous is a common impurity present in biomass-derived synthesis gas, and manganese has been documented to improve light olefin product selectivity. The cobalt-based catalysts were promoted with rhenium and manganese, while the support materials used were γ-Al_2O_3 and two different SiO_2-supports. All catalysts were synthesized by incipient wetness impregnation.

The γ-Al_2O_3-supported catalyst had higher cobalt dispersion and catalyst stability compared to the SiO_2-supported catalysts. The SiO_2-supported catalysts displayed higher C_{5+} product selectivity and higher α-olefin/paraffin ratios than the γ-Al_2O_3-supported catalyst, suggesting that hydrogenation reactions with cobalt supported on SiO_2 are hindered, leading to a higher chain growth probability and higher quantity of olefinic products. Three different loadings of manganese (1.5, 3.75, and 5wt%) were tested on SiO_2-supported catalysts, where light olefin selectivity increased with increased manganese promotion. It was also suggested that an Mn/Co ratio of 0.1 increases the CO conversion of the catalyst. Phosphorous (1700 and 6700 ppmw) was introduced ex-situ to the catalyst by incipient wetness impregnation. The phosphorous contamination significantly reduced the catalyst activity and negatively affected the properties of the cobalt catalyst.

Sammendrag

Dagens globale energiscenario og klimakrise motiverer utnyttelse av fornybare ressurser for å erstatte fossilt brensel. Biomasse er en av de mest lovende karbonnøytrale fornybare ressursene tilgjengelig for bærekraftig produksjon av biodrivstoff og viktige kjemikalier. Biodrivstoff kan lages fra en sekvens av prosesser hvor biomasse først er gassifisert til syntesegass for deretter å bli konvertert til drivstoff via den katalyserte Fischer-Tropsch-prosessen. Syntesegassen fra biomasse inneholder en rekke urenheter som kan forårsake komplikasjoner for den sensitive Fischer-Tropsch-katalysatoren. Fischer-Tropsch-syntesen produserer et bredt spekter av hydrokarboner, hvor en av dem er lette olefiner som er en av de mest essensielle kjemiske mellomproduktene for mange industrier.

I denne studien er effekten av bæremateriale, mangan-promotering og fosfor-kontaminering for kobolt-baserte Fischer-Tropsch-katalysatorer studert. Fosfor er en vanlig urenhet til stede i syntesegass fra biomasse, og mangan er en promoter som er blitt dokumentert å fremme produkt-selektiviteten til lette olefiner. Kobolt-katalysatorene i dette prosjektet var promotert med rhenium og mangan, og bæremateriale som ble brukt var γ-Al_2O_3 og to forskjellige SiO_2-materialer. Alle katalysatorer ble syntetisert ved "incipient wetness" impregnering.

Katalysatoren med γ-Al_2O_3 som bæremateriale viste høyere fordeling av kobolt-atomer og bedre stabilitet sammenliknet med SiO_2-katalysatorene. Katalysatorene med SiO_2 viste høyere C_{5+} produkt selektivitet og høyere α-olefin/parafin forhold enn katalysatoren med γ-Al_2O_3. Dette kan være en indikasjon på at hydrogenerings-reaksjoner er hindret for kobolt på SiO_2, som kan føre til høyere sannsynlighet for kjedevekst og høyere andel av olefiniske produkter. Tre katalysatorer med forskjellige mengder av mangan (1.5, 3.75 og 5wt%) med SiO_2 som bæremateriale ble syntetisert og testet. Resultatene indikerte at produkt-selektiviteten til lette olefiner økte med økende mangan-promotering. Det ble også foreslått at et Mn/Co forhold på 0.1 øker aktiviteten til katalysatoren i henhold til CO-omdannelse. Fosfor (1700 og 6700 ppmw) ble introdusert til katalysatorer ex situ ved "incipient wetness" impregnering. Kontaminering av fosfor førte til en signifikant reduksjon i katalysator-aktiviteten og hadde en negativ innvirkning på egenskapene til kobolt-katalysatorene.

Table of Contents

List of Figures

List of Tables

List of Symbols

α	Chain growth probability
$1-\alpha$	Chain termination probability
i	Number of carbon atoms
w_i	Weight fraction of chain length i
P	Partial pressure
P_0	Saturation pressure
V	Volume
V_m	Volume at monolayer coverage
C	BET constant
Y	Slope
I	Intersection
A_{total}	Total surface area
A_{BET}	Specific BET surface area
N_A	Avogadro's number
m	Mass
σ	Surface tension
θ	Contact angle
r_{pore}	Pore radius
R	Gas constant
T	Temperature
D_{chem}	Dispersion obtained by H_2-chemisorption
Q_0	Quantity adsorbed intercept of the best fit to the primary, repeat or difference data
W_{atomic}	Atomic weight
SF_{calc}	Calculated stoichiometry factor
M_{ps}	Metal particle size
n	Order of reflection
λ	Wavelength
d	Distance
θ	Angle
τ	Particle dimension
τ_{Co}	Crystallite size of cobalt metal
K	Constant
β	Peak width
D_{XRD}	Dispersion obtained by XRD
ΔG°	Change in Gibbs standards free energy
ΔG	Change in Gibbs free energy

X_{CO}	CO conversion
F_{CO}	Molar flow of CO
$F_{CO,0}$	Initial molar flow of CO
w_{Co}	Cobalt loading
r_{CO}	Reaction rate of CO conversion
S	Selectivity
F_B	Molar flow of component B

List of Abbreviations

BTL	Biomass to liquid
FT	Fischer-Tropsch
CTL	Coal to liquid
GTL	Gas to liquid
R&D	Research and development
CFB	Circulating fluidized bed
EF	Entrained flow
WGS	Water gas shift
HTFT	High temperature Fischer-Tropsch
LTFT	Low temperature Fischer-Tropsch
FCC	Fluid catalytic cracking
LHHW	Langmuir-Hinshelwood-Haugen-Watson
ASF	Anderson-Schultz-Flory
IWI	Incipient wetness impregnation
BET	Brunauer-Emmett-Teller
BJH	Barret-Joyner-Halenda
XRD	X-ray diffraction
TPR	Temperature programmed reduction
TOF	Turnover frequency
STY	Site time yield
DI	Deionised
GC	Gas Chromatography
TCD	Temperature Conductivity Detector
FID	Flame Ionization Detector
PR	Pressure regulator
MFC	Mass-flow controller
LFC	Liquid flow controller
PC	Pressure controller

1 Introduction

1.1 Background and Motivation

This thesis is a continuation of the specialized project completed in the fall of 2021 [1]. Therefore, parts of the introduction, theory, and methods are inspired by previous work.

Increasing environmental concerns and fossil fuel pricing have sparked interest in alternate fuel sources. Fossil fuels are the primary source of energy in today's society, supplying more than 80% of the world's energy consumption [2]. However, continuing the use of fossil fuels is not viable as petroleum reserves are depleting rapidly with the increasing demand from the growing population and worldwide industrialization. In addition, the exhaustive use of fossil fuels is one of the prime reasons for global warming. Renewable carbon resources and transportation fuels are crucial for civilization's sustainability. Biomass is a viable renewable carbon source that can be used to make liquid hydrocarbon fuels and chemicals [3]. Biofuels emit significantly less carbon than fossil fuels and reduce greenhouse gas emissions by 50-100 percent [4]. Bioenergy plays an important role in many scenarios for attaining the Paris goals of limiting climate change. The International Energy Agency (IEA) published an energy scenario in 2021 that projected a 60% increase in bioenergy to reach carbon neutrality by 2050 and limit global warming to 1.5℃ [5]. In 2019, bioenergy accounted for 11.6% of total global energy consumption [6].

Biomass to liquids (BTL) is a process in which biomass is first gasified to synthesis gas (syngas), and then liquid fuels are produced through different technologies, where one of the most developed technologies is the Fischer-Tropsch (FT) synthesis [7]. The FT synthesis is a catalyzed process that converts any syngas (H_2 and CO) into a wide range of hydrocarbons. FT synthesis using coal-derived syngas is a well-understood process to create synthetic gasoline. However, employing biomass-derived syngas as a feedstock introduces a new set of contaminants that could compromise the FT catalyst's performance [4]. Biomass contains impurities such as particulates, tars, and sulfur or nitrogen compounds [8;9;3]. As many of these impurities are poisonous to the FT catalyst, the syngas must be cleaned and conditioned before it may be utilized in FT synthesis. Due to the extensive syngas cleaning acquired, the production cost of biofuels is currently approximately two times higher than fossil fuels [4]. The cost of biosyngas cleaning must be reduced to enhance the economic viability. This may be achieved by developing a catalyst with an extended lifetime and selectivity, and that is susceptible to a wide range of impurities [10;4].

Shifting the product selectivity toward the synthesis of light olefins may also improve the economic viability of BTL plants. Selectivity towards light olefin production is achieved through tailored catalysts and specific operating conditions [11]. Biofuels (C_{5+} products) will still be the main products from the FT synthesis but light olefins represents added value. With global consumption of approximately 150 million tonnes per year, light olefins are one of the most important chemical

intermediates in the synthesis of plastics, fiber, and organic chemical [12]. They are conventionally produced through steam thermal cracking of natural gas or naphtha, a process which accounts for global emissions of more than 300 million tonnes CO_2/year [13]. By substituting the BTL-FT process for steam cracking, a more environmentally friendly production of light olefins is achieved while also increasing the economic feasibility of the BTL plant.

1.2 Scientific Objective

The objective of this project is to study, using biomass-derived syngas, the Fischer-Tropsch synthesis for light olefin production. The aim is to optimize cobalt-based catalysts to shift product selectivity toward light olefins, as well as investigate the impact of potential contaminants from biomass-derived syngas, particularly phosphorous. The three aspects studied in this report are: the effect of catalyst support material, the effect of manganese promotion, and the effect of phosphorous contamination.

This project is done in close cooperation with co-supervisor Oscar Luis Ivanez Encinas and is a part of the Norwegian Centre for Sustainable Bio-based Fuels and Energy (Bio4Fuels). Bio4Fuels [14], led by SINTEF, is a center for Environment-Friendly Energy Research (FME) based at the Norwegian University of Life Sciences. They aim to develop innovative technology realizing sustainable conversion of biomass and organic residues into fuels, chemicals, heat and power.

2 Theory

Parts of this chapter are adapted from the specialization project report from autumn 2021 [1].

2.1 Biomass to Liquid

Biomass to liquid (BTL) is a process where biomass is transformed into liquid fuels (biofuels) through a sequence of processes. These biofuels may be used as transportation fuels, replacing the use of fossil-based fuels. Any organic substance that is available on a renewable basis is classified as biomass. Agricultural crops and residues, forest wastes and residues, and municipal and industrial wastes all fall under this category. Biofuels are carbon-neutral which means it does not release any extra CO_2 into the atmosphere, the CO_2 released when the fuel is burned is equal to the CO_2 absorbed by the biomass making the biofuel [15]. There are several ways to convert biomass to biofuels, but the Fischer-Tropsch (FT) method appears to be the most promising [4], which is a process that converts syngas (H_2 and CO) to liquid fuels. From biomass-derived syngas, the FT process promises a clean, carbon-neutral and sustainable energy source [16].

The main sections of a BTL process, in similarity to CTL (coal to liquid) and GTL (gas to liquid) processes, consist of gasification to syngas, gas cleaning and conditioning, Fischer-Tropsch synthesis, and product upgrading. The BTL process with its sections are illustrated in Figure 2.1 [9].

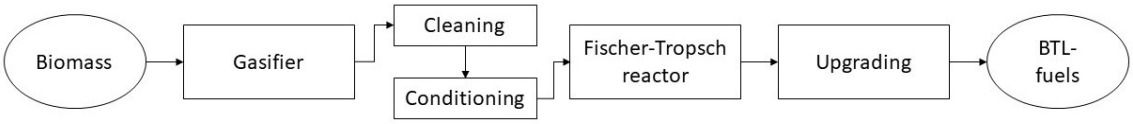

Figure 2.1: Schematic line-up of the biomass to liquid (BTL) process [9].

There are currently no commercial-scale BTL plants, such as those for CTL or GTL. The majority of BTL plants that have been documented are on a demonstration or experimental scale. Several studies have looked into the technical and economic feasibility of various BTL-FT processes to determine the most viable system configuration [17;4;18]. The issues BTL-FT processes are facing include syngas cleaning and conditioning, FT catalyst deactivation, and liquid fuel upgrading to fit into existing infrastructure [4]. It has been suggested that R&D efforts be shifted toward producing an FT catalyst that is more receptive to syngas impurities since this would reduce the high syngas cleaning costs and thus improve economic viability [4;10]. The FT catalyst for BTL-FT processes will be studied and discussed later on in this report.

2.1.1 Biomass Gasification

In the gasifier, biomass is converted into a gaseous mixture of syngas consisting of hydrogen (H_2), carbon monoxide (CO), methane (CH_4) and carbon dioxide (CO_2). Biomass gasification is the partial combustion of biomass with a controlled amount of oxygen at high pressure and temperature (>700℃). Depending on the type of gasification agent (air, oxygen and/or steam) used, different biomass gasification techniques can be utilized [19]. The circulating fluidized bed (CFB) and entrained flow (EF) gasification technologies are determined to be the greatest fit for large-scale BTL plants [17]. CFB gasifiers operate at temperatures between 700 and 1100℃, while EF gasifiers operate at 1200-1400℃. Greater temperatures result in higher carbon conversion, very low tar and methane content, and hence lower syngas cleaning requirements. Both CFB and EF gasifiers are oxygen-blown and pressurized. Oxygen-blown gasification is preferred to air-blown gasification as it results in higher syngas quality [17].

2.1.2 Syngas Cleaning and Conditioning

Syngas cleaning and conditioning are required after biomass gasification as this syngas inevitably contains unwanted impurities such as particulates, tars, sulfur compounds (H_2S), nitrogen compounds (NH_3, HCN), alkali compounds (K, Na) and hydrogen chloride (HCl) [8;9;3]. There are numerous techniques available to provide adequately clean syngas for the FT process.

Particulates may be removed by inertial separation, barrier filtration, electrostatic interaction, or wet scrubbing [3]. Tars can be removed by thermal cracking, catalytic cracking/reforming and wet scrubbing at low temperature using an organic washing liquid. Nitrogen compounds are removed by water adsorption, while H_2S can be removed either by absorption or the Claus process. When condensed, both alkali compounds and HCl may be removed along with particulates and tars through wet scrubbing [3]. To eliminate any remaining H_2S and trace contaminants, the gas can be passed through ZnO and active carbon filters as a final cleaning step [9].

After cleaning, the syngas is conditioned to adjust the H_2/CO ratio to fit the FT synthesis requirement. This conditioning typically includes steam reforming of methane and light hydrocarbons to CO and H_2 over a nickel catalyst, followed by a water gas shift (WGS) reactor. To achieve low quantities of inert gases, the final conditioning step is to remove CO_2 with amine treatment [9].

Almost 75% of the investment costs in a BTL plant are in the process section involving pretreatment, gasification and gas cleaning/conditioning. In an ordinary GTL plant it accounts for 60-70% of the cost, while for a BTL plant this step is 100% more expensive [20]. Syngas cleaning is the biggest challenge for the commercialization of BTL processes. The cleaning step is critical as the catalysts employed in the FT reactor are sensitive to impurities, especially sulfur and nitrogen compounds which irreversibly poison the FT catalysts.

2.1.3 Product Upgrading to Biofuels

The upgrading step is determined by the FT synthesis product distribution as well as the type of biofuel sought. The FT process can be high temperature (HTFT) or low temperature (LTFT). The major product from HTFT is olefins, while for LTFT it is paraffins as well as large amounts of high boiling, waxy products [9]. These waxes may be upgraded to diesel and gasoline. Diesel is obtained from BTL wax by hydrocracking, while fluid catalytic cracking is used to make gasoline. Gasoline can also be produced by upgrading naphtha, a byproduct of the BTL-FT process. The processes for upgrading BTL naphtha include either isomerization or reforming [9].

2.1.4 Light olefin production from BTL-FT

Light olefins play a crucial role in the petrochemical industry. Plastics, synthetic fiber, solvents, packaging materials, coatings, and other end markets are served by their broad range of derivatives [21]. The two most important light olefins are ethylene (C_2H_4) and propylene (C_3H_6), with ethylene being the largest and propylene being the second-largest petrochemicals in the world [22]. Steam cracking of a variety of petroleum feedstocks is the principal source of ethylene [21]. Steam cracking is a process with a high initial investment cost and low expansion potential. Propylene has traditionally been produced as a by-product of the steam cracking of ethylene, and by fluid catalytic cracking (FCC) of gasoline [23].

Demand for light olefins is continuously expanding at a pace of 3-4% per year, driven by rising living standards, and is likely to continue for the foreseeable future [22]. To meet this demand while reducing the dependency on petroleum feedstock, alternatives for light olefin production must be developed [24]. One alternative for light olefin production is through the BTL-FT process. The FT synthesis is the only process that can directly convert syngas to light olefins. In addition, FT liquid products can undergo cracking to obtain light olefins [25]. Seeing as light olefins is such a valuable product for the large chemical industry, making this a main product from the BTL-FT process can increase its viability.

2.2 Fischer-Tropsch

The FT process is named after the two German coal researchers Franz Fischer and Hans Tropsch who in 1923 reacted syngas over a cobalt catalyst, resulting in the production of a wide range of hydrocarbons. This process was widely employed on a commercial scale in Germany for the generation of fuels from coal-derived gas before and during World War II [26]. Today, the FT process is a well-established and mastered technique for the conversion of syngas to higher hydrocarbons, producing both valuable chemicals and liquid transportation fuels [16].

The FT process is typically performed in a fixed-bed reactor using syngas with the 2:1 H_2/CO ratio at 10-60 bar and 200-350℃ [2]. FT may also be performed in fluidized-bed reactors and three-phase slurry reactors [9]. Multitubular fixed bed reactors and slurry-phase reactors are classified as LTFT reactors, while fluidized bed reactors are HTFT reactors. An important quality of FT reactors is to be efficient at heat removal due to the catalyzed FT reaction being highly exothermic [26].

2.2.1 Fischer-Tropsch Chemistry

The FT reaction is considered to be a surface polymerization reaction. Firstly, the reactants, CO and H_2, adsorb and dissociate at the catalyst surface and react to form a chain initiator [27], followed by chain propagation, chain termination and product desorption. A step-by-step addition of CH_2 monomers into the growing chain, as shown in Equation 2.1, can be used to explain the FT product distribution [16].

$$2n\mathrm{H_2} + nCO \rightarrow -(\mathrm{CH_2}) - +n\mathrm{H_2O} \quad \Delta H^\circ{}_{250℃} = -158.5kJ/mol \tag{2.1}$$

Although the chemistry of the FT synthesis is complicated, the essentials can be described using generalized stoichiometric equations. The formation of alkanes, Equation 2.2, and alkenes, Equation 2.3, are the main reactions taking place in the synthesis, where water is the prevailing oxygenated product [28].

$$nCO + (2n+1)H_2 \rightarrow C_nH_{2n+2} + nH_2O \tag{2.2}$$

$$nCO + 2nH_2 \rightarrow C_nH_{2n} + nH_2O \tag{2.3}$$

The ratio of H_2 and CO consumption determines the overall stoichiometry of the FT process. Reactions 2.1 to 2.3 are the simplified versions of several reactions taking place in the FT process. The overall reaction in an idealized BTL-FT synthesis is [16]:

$$2C + \frac{1}{2}\mathrm{O_2} + \mathrm{H_2O} \rightarrow -\mathrm{CH_2} - +\mathrm{CO_2} \tag{2.4}$$

The water-gas shift (WGS) reaction (Equation 2.5), formation of alcohols (Equation 2.6), and the Boudouard reaction (Equation 2.7) are the main side reactions of the FT synthesis [26].

$$CO + H_2O \rightleftarrows CO_2 + H2 \tag{2.5}$$

$$nCO + 2nH_2 \rightarrow H(CH_2)_nOH + (n-1)H_2O \tag{2.6}$$

$$2CO \rightarrow C + CO_2 \tag{2.7}$$

Thermodynamically, both hydrocarbons and alcohols are likely to be formed in the FT synthesis. The choice of catalyst and process conditions are therefore very important to obtain the maximum yield of the most desirable product composition. FT synthesis yields a wide range of hydrocarbon products with varying chain lengths and molecular weights and does not refer to a single product [29;26]. The right catalyst, temperature, pressure and H_2/CO ratio can allow different ranges of hydrocarbon distributions to be synthesised [26].

2.2.2 Fischer-Tropsch Reaction Mechanism

The mechanistic and kinetic factors strongly influence the formation of FT products [16]. The reaction mechanism for FT synthesis is a complicated and well-studied subject. The intricacy and ambiguity of the mechanisms involved, as well as the high number of different species, pose a challenge in defining the FT reaction kinetics [30]. Most kinetic studies describe the overall reactions using empirical power-law expressions, but the mechanism has also been explained using Langmuir-Hinshelwood-Haugen-Watson (LHHW) kinetics [16].

The mechanism that is most widely acknowledged for describing the FT synthesis is the alkyl mechanism. However, the alkenyl, enol and CO-insertion mechanisms are also possibilities. A schematic representation of the alkyl mechanism can be seen in Figure 2.2 and Figure 2.3. The chain initiation occurs by CO being dissociative chemisorbed to the catalyst, forming surface carbon and oxygen. The surface oxygen reacts with either adsorbed hydrogen or CO, yielding water or CO_2, respectively. The surface carbon is hydrogenated, forming CH_2 and CH_3 surface species. CH_2 is referred to as the monomer, while CH_3 is the chain initiator. The chain growth, also referred to as propagation, occurs by successive incorporation of the monomer to the chain initiator. Further, the products are formed/terminated by either β-hydride elimination yielding α-olefins or by hydrogen addition yielding n-paraffins as primary products [31;32]. The H_2/CO ratio (typically 2:1) plays a big part in the FT synthesis. Low partial pressure of CO deters chain-growth and enhances the desorption of olefins [33], while high partial pressure of H_2 favors the chain-termination to paraffins [2].

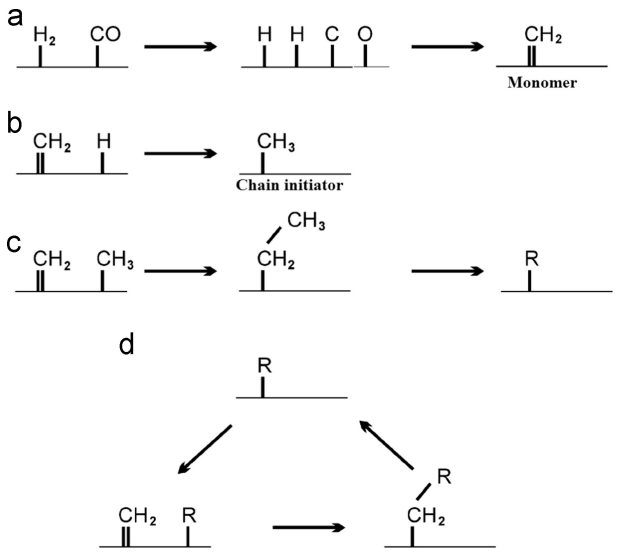

Figure 2.2: Schematic illustration of the alkyl mechanism: (a) methylene formation; (b) chain initiation; (c) chain growth; and (d) propagation [34].

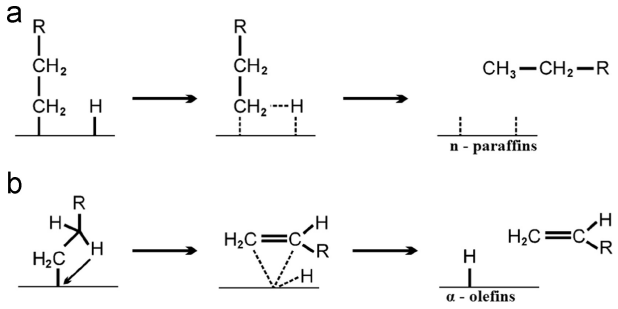

Figure 2.3: Alkyl mechanism for termination of hydrocarbon chains: (a) surface hydride termination yielding alkanes and (b) β-elimination mechanism yielding α-olefins [34].

The α-olefins formed by termination can also reabsorb with chain initiation forming higher hydrocarbons, as well as undergo second hydrogenation forming n-paraffins [35;36]. This is commonly referred to as secondary reactions. Figure 2.4 illustrates the termination possibilities. The chain growth is represented at the bottom of the illustration, where n denotes the number of carbon atoms and * indicates adsorption to the catalyst surface.

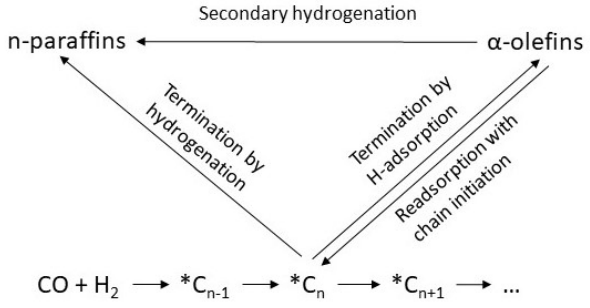

Figure 2.4: Illustration of the FT synthesis showing product termination, readsorption, and hydrogenation of olefins forming paraffins [35].

The carbon number distribution of FT products can be predicted by a simple statistic model called the Anderson-Schultz-Flory (ASF) distribution [26], as shown in Equation 2.8. To follow the ASF model, the relative probability of chain growth (α) and chain termination (1-α) is assumed independent of the chain length and hence constant for all values of minimum chain length. In Equation 2.8, the number of carbon atoms is represented as i, and w_i is the weight fraction of chain length i. α is the probability of chain growth, and $(1-\alpha)$ is the probability of chain termination.

$$w_i = i(1-\alpha)^2\alpha^{i-1} \tag{2.8}$$

When applying the ASF model, the product distribution according to chain growth probability can be illustrated as shown in Figure 2.5. α is very much dependent on the catalyst used and can be modified by the operation conditions. Higher temperature and lower pressure will decrease the chain growth probability, yielding shorter carbon chains [26].

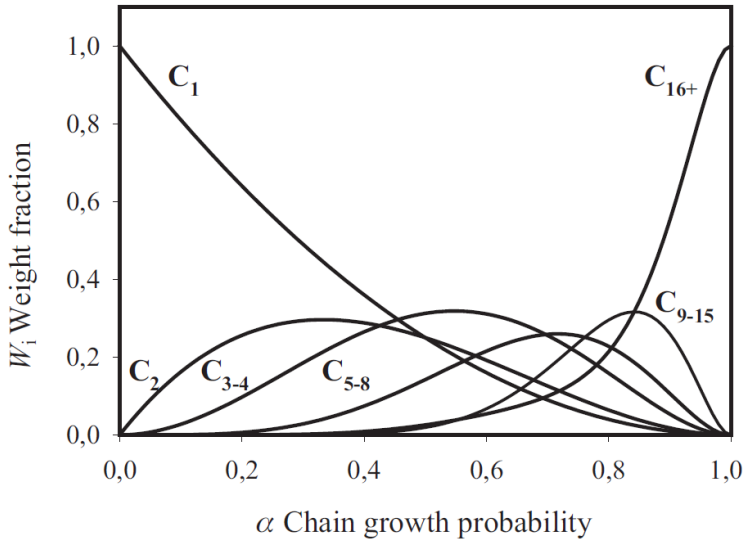

Figure 2.5: Weight fraction as a function of chain growth probability (α) [37].

2.2.3 Process Conditions for Light Olefin Selectivity

Process conditions of the FT synthesis, such as temperature, pressure and H_2/CO ratio, can be altered to shift the product selectivity towards light olefins. According to the ASF chain growth probability (Figure 2.5), an appropriate α-value for optimal light olefin production would be 0.45. Conventional Co-based FT processes are operating by maximizing α. A way of reducing α is to increase temperature and/or decrease pressure. However, this comes with the side effect of increased methane selectivity, the least desired product in FT synthesis [11;38]. An increase in temperature may lower the surface concentration of -CH_2-monomers, resulting in decreased olefin/paraffin ratios, indicating a higher rate of olefin hydrogenation [39].

It has been reported by several, that a lower H_2/CO ratio increases olefin selectivity in FT synthesis [38;40;41]. A low H_2/CO ratio gives an increased surface coverage of CO and a decreased

coverage of H, which will inhibit hydrogenation of olefins to paraffins and other secondary reactions [42]. Increased space velocity (i.e. decreased CO conversion) has also proved to increase olefin selectivity [38] by decreasing the rate of secondary reactions [43]. Because water is the major product of the main FT reactions, the effect of water on olefin selectivity has also been explored [38;44;45;46]. The results of feeding water to the FT synthesis indicated an increase in olefin selectivity with the suggestion that water inhibits hydrogenation and facilitates olefin desorption.

2.2.4 Fischer-Tropsch Catalysts

A FT catalyst requires high hydrogenation activity as its task is to catalyze the hydrogenation of CO to higher hydrocarbons. There are four transition metals that possess this trait and are efficient enough for FT synthesis: iron (Fe), cobalt (Co), nickel (Ni) and ruthenium (Ru) [33]. The easy availability and low cost of iron make it the most used catalyst for FT synthesis. Cobalt is documented to display larger activity than iron as it has significantly higher FT turnover rates [47]. Ruthenium has the highest activity for FT reaction but is the most expensive out of the four. Nickel too have very high activity, however, it produces much more methane than the others, and it forms volatile carbonyl resulting in loss of catalytic material. These factors make Ru and Ni unsuitable for large-scale applications. Hence, Fe and Co are the only two ideal metals that can be used for practical application of FT synthesis, where Co catalysts are preferred over Fe catalysts [16;2].

One big difference between cobalt and iron catalysts is that iron promotes the WGS reaction, making it suitable for low H_2/CO ratios. Cobalt does not have activity for the WGS reaction and requires higher H_2/CO ratios [48]. For this reason, iron is conventionally suited for coal-derived syngas, while cobalt is more suited for syngas derived from natural gas [26]. Biomass-derived syngas can be H_2 deficient, thus demanding a WGS reactor before the FT reactor for Co-based FT synthesis [16]. The WGS activity of Fe catalyst varies a lot, where it in some cases can lead to a 20-50% rejection of carbon feed as CO_2 [16]. Due to negligible WGS activity over cobalt catalysts, the water produced does not affect CO conversion.

With Fe catalysts, FT reactions exist over temperature ranges from 210 to 350°C. At high temperatures (above 250°C), Co catalysts excessively form CH_4. Hence, Co catalysts are only paired with low temperatures (below 200°C) where CH_4 selectivities are less than 15% along with reduced metal- and site-time yields [16].

For the experimental analysis of this project, cobalt-based catalysts are chosen over iron as it has higher activity, selectivity and stability in the synthesis of linear hydrocarbons [49;16]. These qualities yield high productivity which is important for the economic viability of biomass applications.

When selecting a catalyst, it's also critical to consider the catalyst's porosity, pore size, and particle size. The diffusion rate of the FT reaction is very much dependent on these factors as

well as species concentration and the presence of higher hydrocarbons such as liquid waxes [16]. In addition to intrinsic rates, the diffusion rate of reactants and products across the porous catalyst particles determines the overall FT reaction rate. For catalysts with a particle diameter greater than 0.5mm, intra-particle diffusion plays a crucial factor in the FT reaction and is thus a critical parameter for consideration while selecting catalyst particle size and shape, especially for fixed-bed FT processes [50].

2.2.5 Catalyst Promoters and Support Materials

Promoters are commonly added to FT catalysts to improve their properties. The promoter elements can roughly be divided into two categories: structural and electronic. Structural promoters affect the formation and stability of the catalyst's active phase, while electronic promoters directly affect the intrinsic properties of the catalyst by influencing the local electronic structure of the active metal [37]. Noble metals, such as Pt, Re and Ru, are structural promoters often added to Co FT catalysts to decrease the reduction temperature of Co [51;16].

Manganese (Mn) has been identified as a promoter able to increase olefin selectivity in FT synthesis [52;25;53]. Mn has also been reported to increase catalytic activity, Co dispersion, C_{5+} selectivity and decrease CH_4 selectivity for Co-based FT catalysts [11]. However, published results vary from having negative impacts to having no affects to merely activity effects, depending on the support materials, pre-treatment, Mn/Co ratios, and preparation procedures used [54;55;56]. Mn functions as a structural as well as an electrical promoter. Structurally, Mn can reduce Co-particle size, enhance dispersion and aid Co-reducibility [57]. Under FT conditions, Mn is an oxidic promoter that exists in the +2 oxidation state as MnO or as a mixed molecule with Co or the support. The electronic promoting MnO species acts as an electron acceptor from the electron-donating Co, resulting in increased CO dissociation and increased surface coverage of H scavenging carbon monomers [58].

To achieve low metal loading and maximum accessible surface area, the catalytic metal (Co) and promoters are typically dispersed onto support materials. The support material should possess qualities such as high porosity and a large surface area to create a big interface area between the gas phase and the catalytic metal [37]. Commonly used support materials for FT catalysts are Al_2O_3, SiO_2 or TiO_2, and the ratio of Co metal loading is usually in the range of 10-30 g per 100 g of support [33;16].

This project uses a Co-based catalyst promoted with Re to lower the Co-reducibility and Mn to increase olefin product selectivity. The Co, Re and Mn are dispersed on a SiO_2 support material with high porosity and large surface area.

2.2.6 Catalyst Deactivation from Syngas-Impurities

Deactivation of the catalyst can occur for a variety of reasons, with poisoning, carbon formation, and structural changes in the catalyst surface being the three main categories of deactivation [35].

Impurities in the feed are usually the cause of poisoning, which in the case of biomass-derived syngas is very likely if the syngas cleaning is not thorough enough. The deactivation occurs by contaminants binding themselves onto the active sites through chemisorption [35]. The influence of the following syngas contaminants on FT catalysts have previously been investigated by several [59;60;61]: alkali earth metals (Li, Na, K), alkaline earth metals (Ca, Mg), Mn, Fe, P, Cl, H_2S, $(CH_3)_2S$, and NH_3. *Borg et al.* [59] impregnated the catalyst with 100-1000 ppm of the impurity element from nitrate precursors, and the poisoning effect was shown to decrease in the following order: Na > Ca > K > Mg > P. The impact of alkali and alkaline earth metals [60] were stronger than any stoichiometric blocking of surface sites and might be related to the strong electronegativity of the elements preventing CO dissociation. Mn, Fe, and Cl had only minor effects. Sulfur addition (H_2S and $(CH_3)_2S$) to the syngas resulted in deactivation, which was consistent with stoichiometric cobalt surface site blocking [59]. Small quantities of ammonia (NH_3) in the syngas did not affect the FT synthesis activity or selectivity.

Carbon formation is a potential problem in all processes where hydrocarbons or CO/CO_2 are exposed to high temperatures in reducing conditions such as the FT process [35]. Carbon formation, also known as coke formation, deactivates the catalyst by physically blocking active sites on the catalytic surface.

Besides poisoning and coke formation, expected deactivation mechanisms for FT synthesis are re-oxidation of cobalt active sites, carbidization, surface reconstruction, sintering of cobalt crystallites, metal–support solid-state reactions and attrition [62]. Because the cobalt metal is only active in a reduced state, re-oxidation of cobalt active sites will deactivate the catalyst. Carbidization occurs when active sites are lost to form inactive carbides. Although cobalt carbidization is seen as a deactivating feature, recent studies [63;64;65] have found that carbidized cobalt may be beneficial in FT synthesis for the formation of shorter hydrocarbon chains, potentially increasing the selectivity of light olefin products.

Although possible, deactivated cobalt catalysts are difficult to regenerate. This requires various combinations of wax removal, hydrogenation and carbonaceous deposit burning, followed by re-reduction [66]. Carbon deposits covering the catalytic surface and re-oxidation of the cobalt metal are the main causes of catalyst deactivation in the FT process [66;16].

2.3 Catalyst Synthesis

2.3.1 Incipient Wetness Impregnation

Incipient wetness impregnation (IWI) is one of the most often utilized catalyst preparation methods in the industry. IWI, also known as capillary impregnation or dry impregnation, is a simple and cost-effective method of impregnation. Pore volume impregnation, drying, and thermal treatment are the three primary processes in IWI [67].

The IWI method is used for the preparation of heterogeneous catalysts. The active metal precursor is usually dissolved in an aqueous or organic solution, whereas the catalyst support material is usually a porous solid in powder form [67;68]. The support's pore volume must be known so that the amount of metal-containing solution may be calculated to match and not exceed the pores' maximum volume. The aqueous or organic solution is dropwise added to the support and mixed to reach a homogeneous distribution of the solution. During this impregnation step, the solution is adsorbed into the pores by capillary action. The capillary force ensures a uniform distribution. The solubility of the precursor in the solution usually limits the maximum loading of metal on support [68].

2.3.2 Drying and Calcination

The catalyst is dried and calcined after impregnation to extract water and volatile components from the solutions, leaving just the metal on the support.

To remove moisture from the impregnation step, the sample is dried. To ensure that the physical properties of the sample do not change during drying, it is necessary to keep elements like temperature, time, and gas flow rate constant. Only if all of the liquid evaporates spontaneously can uniform distribution be achieved, which is rarely the case. This could affect the dispersion of active components [69].

The sample is calcined once it has dried. Calcination is a thermal treatment that takes place in an oxidizing environment with the goal of stabilizing the physical and chemical properties of the catalyst or its precursor. Gases (typically air) are in direct contact with the sample during calcination [69]. The temperature applied is normally somewhat higher than the catalyst operation temperature to avoid any structural or chemical changes linked to temperature during operation. Thermally unstable substances like carbonates, hydroxides, and organic compounds break down and are usually converted to oxides. New compounds may develop, especially at higher temperatures. Crystallization can occur in amorphous materials. Pore structure, as well as physical and mechanical properties, can alter [69].

2.4 Catalyst Characterization

2.4.1 N_2 Physisorption

N_2 physisorption is used to measure the catalyst surface area and porosity. The method of finding the surface area is typically based on Brunauer, Emmett and Teller's (BET) model [37]. This model describes molecular adsorption and is an extended version of Langmuir's kinetic theory of multilayer adsorption. Liquid phase nitrogen at -196℃ is absorbed onto the surfaces of the sample. It is possible to measure the number of adsorbed nitrogen molecules at monolayer coverage when assuming the occupancy area of the nitrogen molecules equals the cross-sectional area of the sample molecule. The internal surface area can be determined using this information.

The BET equation is given in Equation 2.9 [70], where P represents the partial pressure of nitrogen and P_0 is the saturation pressure. V is the volume adsorbed at P, V_m is the volume adsorbed at monolayer coverage, and C is the BET constant. The BET constant, as well as the adsorbed volume V_m, can be found by plotting Equation 2.9. The slope (Y) and intersect (I) will give the relationships given in Equation 2.10 and Equation 2.11. From these relationships, the total surface area A_{total} and specific surface area A_{BET} can be found by Equation 2.12 and Equation 2.13, where "$_A$" denotes the cross-sectional area of the absorbed molecule, N is Avogadro's number, and m represents the mass of the sample.

$$\frac{P}{V(P_0 - P)} = \frac{1}{V_m C} + \frac{(C-1)P}{V_m C P_0} \tag{2.9}$$

$$V_m = \frac{1}{Y + 1} \tag{2.10}$$

$$C = 1 + \frac{Y}{I} \tag{2.11}$$

$$A_{total} = \frac{V_m N_A}{V} \tag{2.12}$$

$$A_{BET} = \frac{A_{total}}{m} \tag{2.13}$$

Multiple assumptions are behind the theory of Brunauer, Emmett and Teller and the BET-isotherm. The first one is that there is a dynamic equilibrium between adsorbate and adsorptive. Molecules adsorb on equivalent adsorption sites for the first layer, and molecules on the first layer are the adsorption sites for the next layer, and so on. Adsorbate-adsorbate interactions are ignored, and the adsorption-desorption conditions are the same for all layers except for the first. The adsorption energy equals the condensation energy for molecules in the 2^{nd} and higher layers. The final assumption is that the multilayer grows to infinite thickness at saturation pressure [70;37].

The pore size distribution can be determined with the same type of equipment as for the BET using the theory of Barret, Joyner and Halenda (BJH) [71]. The BJH theory is based on the Kelvin equation, shown in Equation 2.14, for the capillary condition in pores. The method involves measuring the adsorption volume in the inclining or declining part of the BET adsorption plot.

$$ln(\frac{P}{P_0}) = -\frac{2\sigma V cos\theta}{r_{pore} RT} \tag{2.14}$$

For Equation 2.14, P and P_0 represents measured pressure and saturation pressure, respectively. σ denotes the surface tension of liquid nitrogen, V is the molar volume of liquid nitrogen, θ represents the contact angle, r_{pore} is the radius of the pore, R is the gas constant, and T is the temperature in Kelvin.

2.4.2 H_2 Chemisorption

Chemisorption is short for chemical adsorption and is referred to as a catalyst characterization method used to measure the dispersion and particle size of a catalyst [37]. The relative efficiency of a catalyst is determined by finding the active surface area of the catalytic material, where the active areas are the areas capable of forming a chemical bond with the adsorptive gas. Hydrogen (H_2) is typically applied as the adsorptive gas, but carbon monoxide (CO) is also a common option [72].

The H_2 gas rapidly forms a monolayer on the catalyst sample and selectively interacts with the active catalytic metals by forming chemical bonds. The quantity of H_2 chemisorbed for each injection is found by subtracting the amount H_2 not adsorbed from the amount injected. Injections are timed for different pressures making an isotherm of quantity H_2 adsorbed versus pressure data points at a constant temperature. This chemical adsorption isotherm is described by the Langmuir isotherm and is used to evaluate the active areas of the catalyst [72]. The Langmuir isotherm model explains adsorption by assuming an adsorbate behaves as an ideal gas at isothermal conditions. Under these conditions, the adsorbate's partial pressure is related to the volume adsorbed onto a solid adsorbent with full monolayer coverage. Through the Langmuir isotherm, the dispersion of active metals on the catalyst surface as well as the particle size of the active metal can be calculated as shown in Equation 2.15 and Equation 2.16, respectively. The calculations are based on the H_2 uptake and the total amount of cobalt in the sample, with a ratio of one molecule of H_2 per two atoms of cobalt. The cobalt particles are assumed spherical and uniform.

$$D_{chem} = \frac{100\% \cdot 100\%}{22414} \cdot \frac{Q_0 \cdot SF_{calc}}{\frac{\%weight}{W_{atomic}}} \tag{2.15}$$

$$M_{ps} = \frac{96}{D} \tag{2.16}$$

D_{chem} represents the metal dispersion (%) measued by the H_2-chemisorption. $\%weight$ is the % of sample weight for the metal. Q_0 is the quantity adsorbed intercept of the best fit to the primary, repeat, or difference data. W_{atomic} is the atomic weight of the metal (g/mole). SF_{calc} is the calculated stoichiometry factor. 22414 is the volume one mole of gas occupies (cm^3 STP/mole of gas). M_{ps} represents the metal particle size (nm).

2.4.3 X-ray Diffraction

X-ray diffraction (XRD) is a method used for identifying crystallite phases and crystallite particle sizes using lattice structural parameters [37]. X-ray diffraction occurs in the elastic scattering of X-ray photons by atoms in a periodic lattice. The scattered monochromatic X-rays give constructive interference. Various X-rays by different planes allow the lattice spacings to be derived using the Bragg relation shown in Equation 2.17. n represents an integer for the order of the reflection, λ is the wavelength of the X-rays, d is the distance between two lattice planes, θ is the angle between the incoming X-rays and the normal to the reflection lattice plane. Equation 2.17 can be used to obtain an XRD pattern of the catalyst sample, showing the intensity of the signals characteristic to the crystallite phases as a function of 2θ.

$$n\lambda = 2dsin\theta \tag{2.17}$$

The particle size of the crystallites can be found by the Scherrer formula shown in Equation 2.18, which relates crystal size to the line width [37]. τ is a measure of the dimension of the particle in the direction perpendicular to the reflecting plane, K is a constant often taken as 1, λ is the X-ray wavelength, β is the peak width, and θ is the angle between the beam and the normal to the reflecting plane.

$$\tau = \frac{K\lambda}{\beta cos\theta} \tag{2.18}$$

The metal dispersion (D_{XRD}) can be calculated, as shown in Equation 2.19, from the obtained crystallite size (τ), assuming spherical uniform cobalt particles with a site density of 14.6 atoms/nm^2. A reduction factor of 0.75 is included to obtain the crystallite size of metallic cobalt, as τ is a measure of the cobalt oxide for this project.

$$D_{XRD} = \frac{96}{0.75\tau} \tag{2.19}$$

2.4.4 Temperature Programmed Reduction

Temperature programmed reduction (TPR) is a characterization technique used to study the catalyst's reducibility [37]. The reducibility is found through the surface chemistry of metal and metal oxides. A gas stream of a reducing mixture such as hydrogen is sent through the sample under gradually increasing temperature. The linear heating gives a reduction rate correlated with temperature, resulting in a TPR profile. At the outlet, the chemical difference is continuously analyzed in ambient conditions by a highly sensitive detector. These measurements yield a precise representation of the catalyst's maximum or peak reduction rate [73].

The reducing gas mixture (H_2) reduces the catalyst's metal oxide to its metal state and produces water. The most relevant metal oxide for this project is cobalt oxide, which follows a two-step reduction to cobalt metal. These reduction steps are shown in Equation 2.20 and Equation 2.21.

$$Co_3O_4 + H_2 \rightarrow 3CoO + H_2O \tag{2.20}$$

$$3CoO + 3H_2 \rightarrow 3Co + 3H_2O \tag{2.21}$$

Thermodynamically, the reduction is feasible for metal oxides with a negative standard free energy change (ΔG°). But this is not true for all metal oxides, and for this reason, the TPR experimental method constantly removes the water vapor formed by reduction. As seen in Equation 2.22, by lowering the partial pressure of water (P_{H_2O}) at elevated temperatures it is possible to proceed with the reduction even when ΔG° is positive. When the last term, $RTlog(P_{H_2O}/P_{H_2})$, is sufficiently negative enough it may nullify the positive ΔG° [74].

$$\Delta G = \Delta G^\circ + RTlog(\frac{P_{H_2O}}{P_{H_2}}) \tag{2.22}$$

For Equation 2.22, ΔG represents the change in Gibbs free energy, while ΔG° is the change in the standard Gibbs free energy. R is the gas constant and T is the temperature. P_{H_2O} denotes the partial pressure of water vapor and P_{H_2} is the partial pressure of hydrogen gas.

2.5 Catalyst Performance

The purpose of testing the catalyst performance is to discover the optimal catalyst for producing the desired products. When doing catalytic testing, the aim is usually to determine the catalyst activity, selectivity, and stability.

2.5.1 Activity Measurements

Conversion, turnover frequency (TOF), site time yield (STY), reaction rate, and space velocity are a few examples of measurements that can be used to determine catalytic activity. The catalytic activity data in this study is obtained through conversion and STY measurements. Conversion is found by the amount of reactant (in this case, CO) converted divided by the amount of reactant in the feed. STY is calculated by the number of molecules reacting divided by the number of surface atoms (in this case, cobalt atoms) on the catalyst per unit time [37]. The formulas used for calculating the conversion of CO and the STY in this project are given in Equation 2.23 and Equation 2.24, respectively.

$$X_{CO} = 1 - \frac{F_{CO}}{F_{CO,0}} \tag{2.23}$$

$$STY = \frac{r_{CO} \cdot M_{Co}}{w_{Co} \cdot D} \tag{2.24}$$

For Equation 2.23, X_{CO} represents the CO conversion, F_{CO} is the outlet molar flow of CO while $F_{CO,0}$ is the initial molar flow of CO. In Equation 2.24, M_{Co} represents the molar mass of the catalytic metal cobalt, w_{Co} is the cobalt loading, D is the cobalt dispersion found by H_2-chemisorption, and r_{CO} denotes the the reaction rate of CO conversion. The reaction rate r_{CO} is found by Equation 2.25 where $m_{catalyst}$ is the mass of the catalyst.

$$r_{CO} = \frac{F_{CO,0} \cdot X_{CO}}{m_{catalyst}} \tag{2.25}$$

2.5.2 Selectivity Measurements

Selectivity (S) is the ability the catalyst has to produce the desired product. The calculations of selectivity are dependent on temperature, pressure, space velocity, feed composition, reactor geometry, and degree of conversion [37]. Because selectivity is known to be dependent on conversion, all comparisons should be made at the same conversion level [44]. For this project the selectivity was calculated by Equation 2.26 where F_B denotes the outlet molar flow of relevant component B, $F_{CO,0}$ is the total inlet molar flow of CO, and the CO conversion (X_{CO}) is ∼50%.

$$S_B = \frac{F_B}{F_{CO,0} \cdot X_{CO}} \tag{2.26}$$

2.5.3 Stability Measurements

The stability of a catalyst is also referred to as its lifetime. Stability is dependent on catalyst deactivation mechanisms and the catalyst durability under process conditions such as temperature and pressure. A catalyst's lifetime is defined as the amount of time it can sustain sufficient activity and selectivity for the process [37]. Hence, the stability is measured by the catalyst's activity and selectivity over a longer period. The lifetime of a catalyst is critical for commercialization, as a catalyst with high initial activity is not always the best catalyst for industrial application in terms of feasibility.

3 Experimental Methods

Parts of this chapter are similar to the specialization project report from autumn 2021 [1], as many of the experimental methods were the same.

3.1 Catalyst Synthesis

3.1.1 Incipient Wetness Impregnation

The catalysts were prepared by the incipient wetness impregnation (IWI) synthesis method. Deionised (DI) water was used as a solvent for all impregnations. The liquid absorption capacity of the support material was determined by slowly adding DI water to 1 gram of support material until the incipient wetness point was reached. Support materials used were gamma-alumina oxide (γ-Al_2O_3) and two different silicon dioxides (SiO_2), which hereby will be referred to as silica#1 and silica#2. The gamma-alumina oxide was type Sasol Puralox SCCa 45/190 with a BET specific surface area of 175 m^2/g, pore volume of 0.73 cm^2/g and an average pore size of 12 nm. Silica#1 was of Davisil Grade 62 from Sigma-Aldrich with pore size 150 Å, particle size 60-200 mesh, and pore volume 1.15cm^2/g. Silica#2 was of high purity grade from Sigma-Aldrich with pore size 60 Å, particle size 40-75µm, and pore volume 0.7-0.9cm^2/g. All support materials were sieved to achieve particle sizes between 54 and 90µm before impregnation. The precursor of the catalytic material used was cobalt nitrate ($Co(NO_3)_2{\cdot}6H_2O$), while the precursors of the promoters used were manganese nitrate ($Mn(NO_3)_2{\cdot}4H_2O$) and perrhenic acid ($HReO_4$). Impurity components in the syngas can allegedly have a significant adsorption capacity in fixed-bed reactor lines. In the case of phosphorous, when adding it to the syngas flow, there is also a possibility of the highly poisonous gas phosphine being formed, which is immensely undesired. Therefore, catalyst samples were ex situ-modified by impregnation, where the precursor phosphoric acid (H_3PO_4) was added post-impregnation.

The impregnation of the different precursors to the support material proceeded in several IWI steps, which is illustrated in Figure 3.1. The first sequence shows the synthesis of the reference catalyst which followed just one impregnation step. Cobalt and rhenium were impregnated onto the support material before being dried and calcined, yielding the reference catalyst. The methods used for drying and calcination are described in the next section. The second sequence illustrates a two-step impregnation method for the synthesis of catalysts with manganese promotion. Here the support was impregnated with a manganese nitrate solution before the sample was dried and calcined. Then the cobalt nitrate and perrhenic acid solution were impregnated on the calcined sample followed by an additional drying and calcination step, resulting in the desired catalyst. The third sequence shows how the phosphorus-containing catalysts were synthesized in a three-step impregnation method. Normally parts of the catalyst synthesized in the second sequence

were used to obtain the phosphorus-containing catalysts. Phosphoric acid diluted in DI water was impregnated onto the catalyst before being dried and calcined a final time.

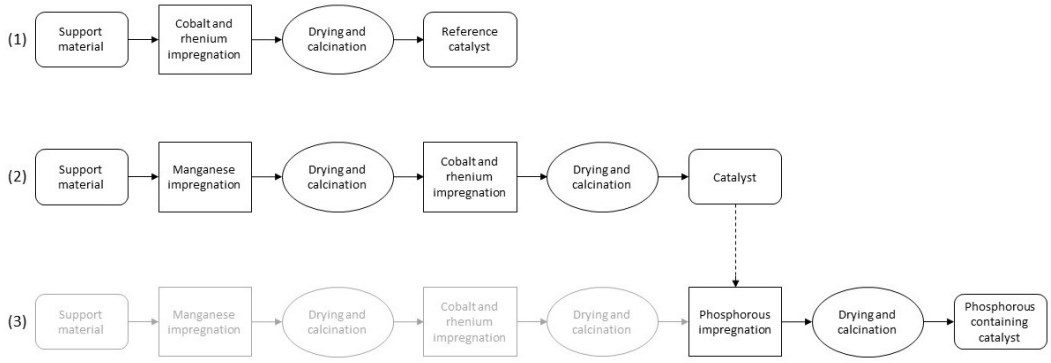

Figure 3.1: Illustration of the sequences for catalyst synthesis yielding the different element containing catalysts: reference catalyst (1), catalyst with manganese promoter (2), and phosphorous-containing catalyst (3).

The desired amount of support material was weighed and added to a large beaker glass. The calculated quantity of manganese nitrate or cobalt nitrate and perrhenic acid was added to a small beaker glass with small amounts of DI water. The metal salts (manganese nitrate and cobalt nitrate) were made sure to be fully dissolved before adding the solution to a volumetric flask where the rest of the DI water was added giving a total volume equal to the liquid absorption capacity of the amount of support used for the catalyst preparation. The phosphoric acid was added to a volumetric flask and diluted with the correct amount amounts of DI water. The concentrations of the impregnation solutions were calculated to obtain catalysts with 15wt% cobalt, 1.5, 3.75, or 5wt% manganese, 0.5wt% rhenium, and 1700 or 6700 ppmw phosphorous. The impregnation solution was slowly and drop-wise added to the beaker containing the support material with manual mixing to ensure uniform wetting of the support material. The incipient wetness point was reached when all impregnation solution was added. The calculations made for the catalyst synthesis can be seen in Appendix A.

3.1.2 Drying and Calcination

The samples were dried in a beaker glass in a ventilated oven at 110°C overnight. During the first two hours, the sample was stirred regularly to ensure uniform drying.

Calcination was performed in an in-house built set up with an in-house built reactor. The reactor was a quartz tube reactor with an inner diameter of 40 mm containing a porous quartz sinter floor to keep the sample in place. The reactor had a Teflon lid where a quartz tube was inserted. The quartz tube was made to hold a thermocouple. The tube with the thermocouple was kept near the surface of the sample. The reactor containing the dry sample was placed in an electrically heated, temperature-controlled furnace. The temperature was controlled by a Eurotherm which received the temperature reading from the thermocouple inserted in the reactor. Calcination proceeded

with flowing air with a sufficient flow rate going through the catalyst bed. Before entering the vent, the airflow was sent through a water trap bottle to inhibit emissions of volatile gases. The temperature program for the calcination had a rate of 2℃/min reaching the target temperature of 300℃. After the target temperature was reached, the calcination proceeded for 16 hours with 300℃ and airflow.

To avoid the possibility of diffusion limitations during experimental analysis, all catalysts were sieved after synthesis, obtaining particle sizes between 53 and 90µm.

3.2 Catalyst Characterization

3.2.1 N_2 Physisorption

N_2 Physisorption was carried out in a Micromeritics Tri Star 3000 Area and Porosity Analyzer, where pretreatment of samples was performed in a VacPrep 061 Degasser unit.

Approximately 100 mg sample was added to a weighed quartz tube designated for the analysis instruments. The sample was degassed under vacuum for one hour at ambient temperature and overnight at 200℃ until the pressure reached below 100 mTorr. The sample weight after degassing was noted.

The physisorption procedure was then executed using the Micromeritics Tri Star 3000 Area and Porosity Analyzer. The dewar for the instrument was filled with liquid nitrogen, and the samples were analyzed at the temperature of liquid nitrogen (-196℃). The BET and BJH methods were used to calculate the surface areas, pore volumes, and pore sizes of the samples.

3.2.2 H_2 Chemisorption

H_2 Chemisorption experiments were performed by a Micrometrics ASAP 2020S instrument, obtaining the dispersion metal particle size of each catalyst.

Approximately 100 mg of sample was loaded in a quartz reactor between two parts of quartz wool. The reactor was connected to the instrument, and a thermocouple was placed outside of the reactor at the height of the sample bed. Degassing under vacuum was performed for at least two hours until the pressure reached below 0.003 mmHg, followed by a leak test. The program for the experiment is listed in Table 3.1.

Table 3.1: H_2 chemisorption sequence performed for all samples.

Task	**Temperature** [℃]	**Time** [**min**]	**Pressure** [**mmHg**]
Evacuation	40	60	-
Leak Test	40	-	0.030
Hydrogen flow	350	960	760
Evacuation	330	60	-
Evacuation	100	30	-
Leak Test	100	-	0.30
Analysis	40	-	-

3.2.3 X-ray Diffraction

XRD experiments were carried out in a Bruker D8 DaVinci X-ray diffractometer instrument with CuKα radiation, a LynxEYE^{TM} SuperSpeed Detector, and a 90 position sample changer. Specifications for the standard powder diffraction set-up are according to Bragg-Brentano geometry.

The sample was crushed with a mortar, achieving a particle size close to 10 microns. A smooth and flat surface of the sample in the sample holder was obtained. The measurements were executed by laboratory technicians. The scan time was set to 30 minutes, while the angular range (2θ) was 15-75°, and the divergence slit was 0.3 degrees. X-ray diffractograms were obtained using a program for crystalline samples with a step size of 0.013°/step.

The EVA software was used to compare the peaks with references in a database to identify the different phases present in the samples. The particle sizes were determined by the software using the Scherrer formula. The crystallite sizes were calculated from the highest peak of the relevant crystal (Co_3O_4) in the diffractograms.

3.2.4 Temperature Programmed Reduction

The TPR analysis was carried out in a BenckCAT Hybrid 1000 HP. A thermal conductivity detector (TCD) measured the H_2 consumption as a function of temperature. The instrument was equipped with a 1/4 inch stainless steel trap containing a dissecant (drierite) which removed water during degassing steps and TPR procedures. The drierite was changed after every third experiment.

Approximately 100 mg of sample was loaded in a U-shaped quartz reactor between two parts of quartz wool. The catalyst bed was made sure to be positioned at a height below the instrument's thermocouple. The analysis was executed after performing a leak test. The conditions of the experiments included flowing 50 mL/min of 7% H_2 in Ar, and a temperature increase up to 800℃ with a ramp rate of 10℃/min.

3.3 Fischer-Tropsch Synthesis

Fischer-Tropsch synthesis experiments were performed using an in-house built laboratory-scale setup. A flowsheet of the setup is provided in Figure 3.2.

The gases (syngas, helium, and hydrogen) used for the experiments were provided in 50L gas bottles at 200bar pressure. The helium (He) and hydrogen (H_2) gases used had e purity of 99.996 and 99.999%, respectively. The syngas was ordered premixed with a H_2/CO ratio of 1.5, containing 3% N_2 to act as the Gas Chromatography (GC) internal standard. The GC employed for the experiments was an Agilent Technologies 6890N containing a packed Carbosieve S-II column with a Temperature Conductivity Detector (TCD) and a GS-Al_2O_3 PLOT column with a Flame Ionization Detector (FID).

The syngas was fed through a PbO trap upstream of the MFC to remove metal carbonyls from the feed gas stream. He and H_2 were fed through moisture- and oxygen traps. Before the Fischer-Tropsch reactor, H_2 was added with a flow controller and mixed with the syngas to achieve the desired H_2/CO ratio of 1.7 to simulate H_2 deficient syngas, which is likely when produced from biomass. The mixed gas feed was heated to approximately 170℃ before entering the reactor. The setup had an option to feed water/steam from the water tank, but this option was not utilized in these experiments.

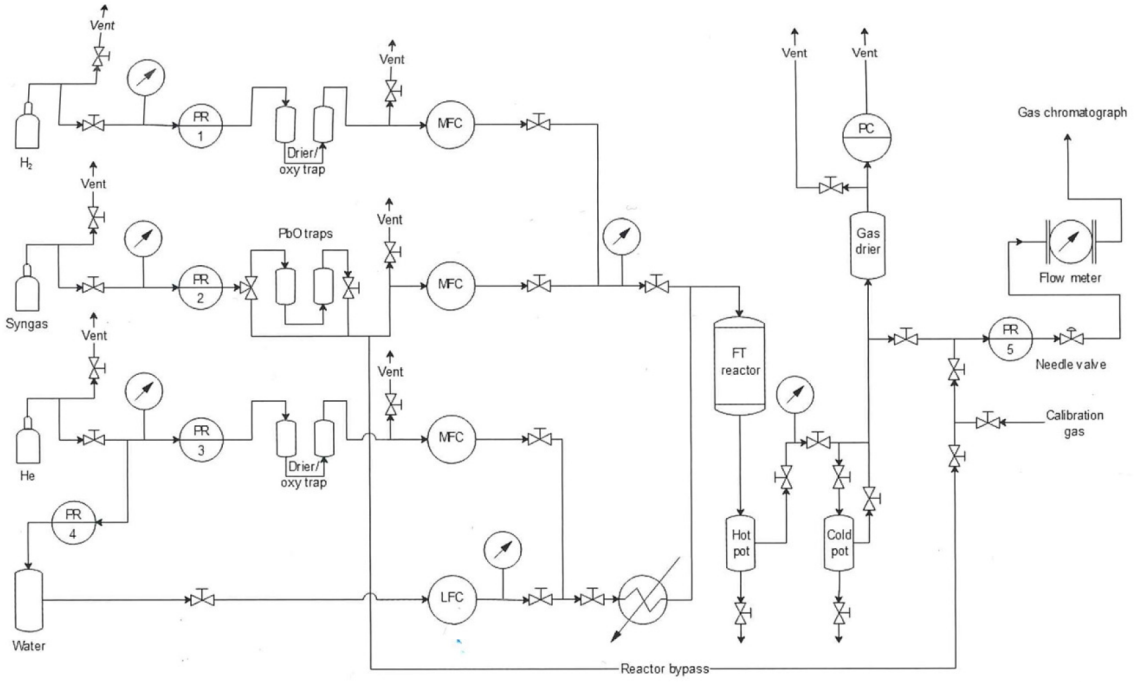

Figure 3.2: Flowsheet of the laboratory Fischer-Tropsch (FT) synthesis in-house built setup, including pressure regulators (PR), mass-flow controller (MFC), a liquid flow controller (LFC), and pressure controllers (PC).

The FT reactor was a stainless steel fixed-bed reactor with an internal diameter of 10 mm. 1 gram of catalyst was diluted with 19 grams of SiC powder before being added to the reactor. The

purpose of this dilution was to reduce temperature gradients. The catalyst mixture was placed in the reactor between two plugs of quartz wool to keep it in place, resulting in a bed length of around 20cm. To further minimize temperature gradients, the reactor was mounted between two alumina blocks which together create a cylindrical aluminum block hugging the reactor. The reactor and alumina block were situated in an electrically heated, temperature-controlled furnace. The reactor, alumina block, and furnace had accurate dimensions to be tightly fitted together. To monitor the temperature inside the reactor a stainless steel thermowell fitted with a thermocouple was inserted through the catalyst bed.

The product gas downstream of the reactor was passed through a hot condenser kept at approximately 90℃ and a cold condenser at ambient temperatures where heavy FT products and water was collected. Small amounts of the product gas after the cold condenser (∼30 NmL/min) were split off and analyzed in the GC. The rest of the product gas was sent through a molsieve type drier and a back pressure controller to control the operating pressure. Catalyst activity and selectivity towards CH_4 and CO_2 were determined by comparing data from the TCD of the GC with calibration data. The hydrocarbon selectivity was determined by comparing the CH_4 selectivity with the FID data from the GC.

All gases used in the experiments were regulated to the operating pressure of 5 bar. A leak test of the setup was performed with He at 20 bar before every experiment. After leak testing, the catalyst was reduced in 125/125 mL/min H_2/He flow at 350℃ for 10 h and cooled to 170℃. The ramp temperature was 2℃/min from ambient temperature to 170℃, and 1℃/min from 170 to 350℃. After the reduction, the temperature was reduced to 170℃, and the reactor was pressurized to operating pressure (5 bar) with 250 mL/min He. When pressurized, the He flow was removed and 250 mL/min of the syngas and H_2 mixture was introduced while the reactor was heated to 230℃ (20℃/min) and 240℃ (5 ℃/min). The GC was turned on as the operating temperature (240℃) was obtained. The catalyst activity (CO conversion) was documented by the GC every hour from 0 to 24 hours on stream. After 24 hours, the syngas and H_2 flow was tweaked to obtain a desired CO conversion level of 50%, and selectivity measurements were obtained for an additional 6 hours. After the 30-hour-long experiment, the reactor was depressurized and cooled with 10 mL/min He.

4 Results and Discussion

Some of the catalysts and results were prepared and obtained during the specialization project of autumn 2021 [1].

Different studies have been carried out in this project. To study the effect of support materials for the production of light olefins, three different supports were used: γ-Al_2O_3, SiO_2#1, and SiO_2#2. The main difference between the silica supports are the pore size, where SiO_2#1 (150 Å) has larger pore sizes than SiO_2#2 (60 Å). To understand the nature of the manganese promotion, silica supported catalysts with different loadings of manganese were synthesized and tested. And finally, to study the effect of phosphorous contamination from biomass-derived syngas on the FT synthesis, different loadings of the poison were deposited in the catalysts and tested. The results of this study will be discussed and presented as follows:

- The effect of support material
- Promoting effect of manganese
- The effect of phosphorous contamination

Table 4.1 provides an overview of all catalysts synthesized and tested for this project. The first column shows the support material used, and the third column is a description of the characteristic of the specific catalyst and the names of which the catalysts may be referred for the rest of the report.

Table 4.1: Overview of all catalysts synthesised and tested for the project.

Support	**Catalyst**	**Name and type of catalyst**
Alumina	$CoReMn/Al_2O_3$	Standard catalyst
Silica #1	$CoRe/SiO_2$	Reference catalyst
-	$CoReMn/SiO_2$	Standard catalyst
-	P1-$CoReMn/SiO_2$	P1 catalyst (1700 ppmw phosphorous)
-	P2-$CoReMn/SiO_2$	P2 catalyst (6700 ppmw phosphorous)
Silica #2	$CoRe/SiO_2$	Reference catalyst
-	$CoReMn/SiO_2$	Standard catalyst
-	$CoReMn/SiO_2$	1.5%Mn catalyst (1.5wt% manganese)
-	$CoReMn/SiO_2$	5%Mn catalyst (5wt% manganese)
-	P1-$CoReMn/SiO_2$	P1 catalyst (1700 ppmw phosphorous)
-	P2-$CoReMn/SiO_2$	P2 catalyst (6700 ppmw phosphorous)

The element distribution for the catalyst synthesis is shown in Table 4.2. The reference catalysts does not containing manganese, and the P1 and P2 catalysts include small amounts of phosphorous in addition to the element distribution of the standard catalysts.

Table 4.2: Element distribution of all catalysts showing the amounts of cobalt, rhenium, manganese and phosphorous impregnated to the supports.

Catalyst	**Co [wt%]**	**Re [wt%]**	**Mn [wt%]**	**P [wt%]**
Reference catalysts	15	0.5	-	-
Standard catalysts	15	0.5	3.75	-
1.5%Mn catalyst	15	0.5	1.5	-
5%Mn catalyst	15	0.5	5	-
P1 catalysts	15	0.5	3.75	0.17
P2 catalysts	15	0.5	3.75	0.67

4.1 The Effect of Support Material

The effect of silica as support material is compared to an alumina-supported catalyst with the same element distribution of cobalt, rhenium and manganese. Both the first and the second type of silica performance will be compared to the alumina as well as to each other to see if their difference in characteristics will affect the catalyst performance.

Surface area, pore volume and pore size were found by the BET and BJH method, and the results from the relevant catalysts and support materials are represented in Table 4.3. High porosity and a large surface area are desired qualities that support materials should possess. Silica#2 has the largest surface area of 492m^2/g, silica#1 has 296m^2/g, and alumina has the smallest surface area of 182m^2/g. For the pore volume, silica#1 has the highest at 1.1cm^3/g, while alumina and silica#2 have approximately the same pore volume of 0.73 and 0.72cm^3/g. The pore size of alumina (13.4 nm) and silica#1 (11.5) is more than twice as big as silica#2 (4.5 nm). Similar to all three, the surface area and pore volume decrease after impregnation of cobalt and promoters. This indicates that the elements are impregnated into the pores of the support materials and that there may be some pore blockage by cobalt or promoter clusters. Pore blockage would expect to change the pore size. The alumina supported catalyst is the only one out of the three that show a decrease in average pore size, indicating pore blockage of larger pores. Figure 4.1 show the change in pore volume with respect to pore width obtained by the BJH method for the catalysts compared to the support material. There appear to be a slight trend of a reduction in wider pores for all catalysts, but the reduction is not large enough to change the obtained average pore size. The results indicate that the Co and promoters are even distributed in the pores.

Table 4.3: Results of surface area, pore volume and pore size obtained by the BET and BJH method for the standard alumina supported catalyst and the standard catalyst for the two different silica support materials.

Catalyst	**Surface area** [m^2/g]	**Pore volume** [cm^3/g]	**Pore size [nm]**
Al_2O_3	182	0.73	13.4
CoReMn/Al_2O_3	143	0.49	11.4
SiO_2#1	296	1.10	11.5
CoReMn/SiO_2#1	236	0.82	11.8
SiO_2#2	492	0.72	4.5
CoReMn/SiO_2#2	389	0.52	4.4

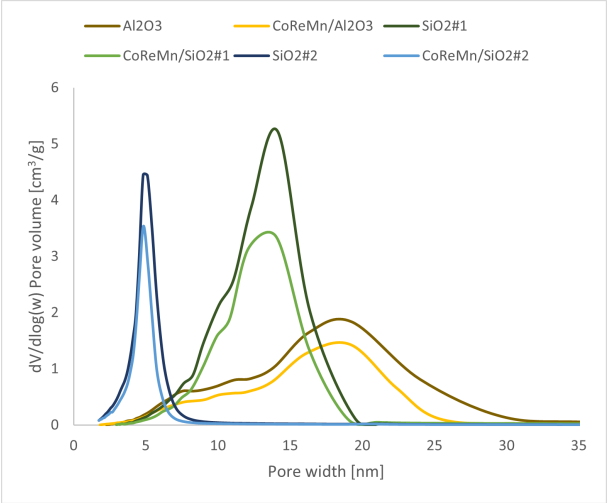

Figure 4.1: The change in pore volume as a function of pore with for the three different supported catalysts compared to the support materials (Al_2O_3, SiO_2#1, SiO_2#2). The results are obtained from the BJH method.

The results obtained by H_2-chemisorption for dispersion and metal particle size are displayed in Table 4.4. The metal particle size is calculated from the dispersion obtained by H_2-chemisorption. The results obtained by XRD including crystallite size and dispersion are also displayed in Table 4.4. The crystallite size is measured from the peak of cobalt oxide with the highest intensity found by XRD, and the dispersion is calculated from the obtained crystallite size. The results for metal particle sizes obtained from H_2-chemisorption and the crystallite size from XRD can be comparable to a certain degree. The XRD crystallite size measures the dimension of the different phases of the metal, while the H_2-chemisorption metal particle size is a measure of the grain. The H_2-chemisorption values are expected to be higher than the XRD values. In the case of the alumina, strong metal-support interactions may form smaller particles than 3 nm which is not detectable by XRD, resulting in an underestimation of the crystallite size. The alumina-supported catalysts have a higher dispersion of 7.8%, while the silica#1 and silica#2-supported catalysts have dispersions of 6.0 and 6.6%. The difference in dispersion might be caused by the different metal-support interactions. Alumina is reported to have stronger interactions with cobalt, while silica exhibit weaker metal-support interactions [75;44]. On the alumina, it is found that the smallest particles are in strong interaction with the support, resulting in the increased metallic dispersion.

Table 4.4: Characterization results for the standard alumina supported catalyst and the standard catalyst made with the two different silica support materials. The results include cobalt dispersion (D_{chem}) and metal particle size (M_{ps}) obtained from H_2-chemisorption, and cobalt dispersion (D_{XRD}) and crystallite size (τ_{Co}) obtained from XRD.

Catalyst	**H_2-chemisorption**		**XRD**	
	D_{chem} [%]	**M_{ps} [nm]**	**D_{XRD} [%]**	**τ_{Co} [nm]**
$CoReMn/Al_2O_3$	7.8	12.2	10.1	9.5
$CoReMn/SiO_2$#1	6.0	16.0	9.3	10.4
$CoReMn/SiO_2$#2	6.6	14.5	12.3	7.8

As cobalt oxide follow a two-step reduction to cobalt metal, the TPR profile is expected to display two distinct peaks. The TPR profile of the three catalysts is shown in Figure 4.2. The first large peak is attributed to the reduction from Co_3O_4 to CoO, and the second large peak is attributed to the reduction from CoO to Co. The first shoulder at around 200℃ is attributed to residues of the nitrate precursor remaining after calcination [76;44]. Because calcination temperatures above 450℃ are needed to completely decompose the nitrate [44], likely, some of it may still be present in calcined samples. The last peak at ∼500℃ most likely represents a broadening of the last reduction step of CoO to Co. A broadening may be due to incomplete initial reduction of CoO or because of different-sized particles giving a varying degree of interaction with the support [77]. The last peak may also be a reduction of Mn occurring almost simultaneously with the reduction of CoO. Another probable mechanism is that there has been formed a $Co_{3-X}Mn_XO_4$ type mixed oxide [78;79] in the catalyst, which is harder to reduce. The precise identity of the species is not clear.

The reduction profiles in Figure 4.2 give a slight indication that interactions with support material influence the reduction of Co_3O_4 to Co. Although minimal, alumina display higher reduction temperatures. As mentioned before, alumina have stronger metal-support interactions with the small cobalt particles, which may decrease the reducibility of the catalysts, shifting the temperatures to higher values.

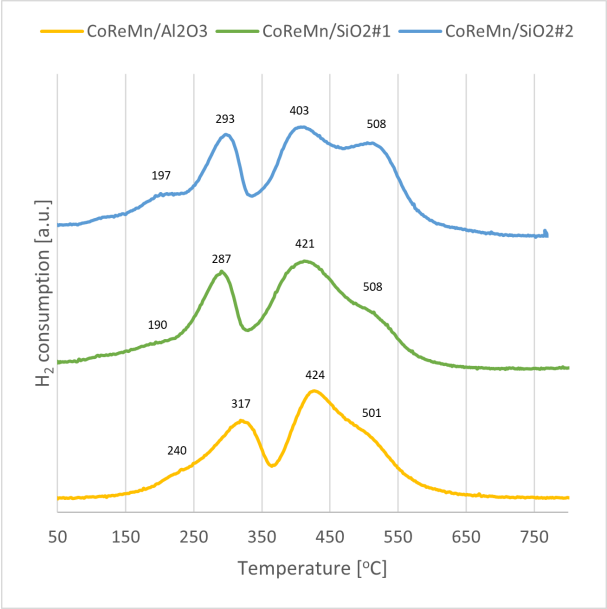

Figure 4.2: TPR profile as H_2 consumption as a function of the bed temperature for the three different supported catalysts (Al_2O_3, SiO_2#1 and SiO_2#2). The reaction conditions were 50 mL/min of 10%H_2/Ar flow and 800ºC (10ºC/min).

Figure 4.3 show the XRD profiles of the three catalysts. The XRD profiles were used to identify the phases of the different species. The catalyst was not reduced before XRD analysis, thus all elements are found in their oxidized form. The XRD revealed that only phases of Co_3O_4, MnO_2, alumina and silica were detected. The rhenium was not present attributed to highly dispersed rhenium resulting in particles smaller than 3 nm. Co_3O_4 was detected at the same degrees for all catalysts. Both Al_2O_3 and SiO_2 were detected, where SiO_2 is present at lower degrees than Al_2O_3. Only small intensity peaks were observed for MnO_2, attributed also to highly dispersed Mn species. No other oxidic faces of the elements were detected, such as MnO or CoO, which suggests that all elements were fully oxidized after calcination.

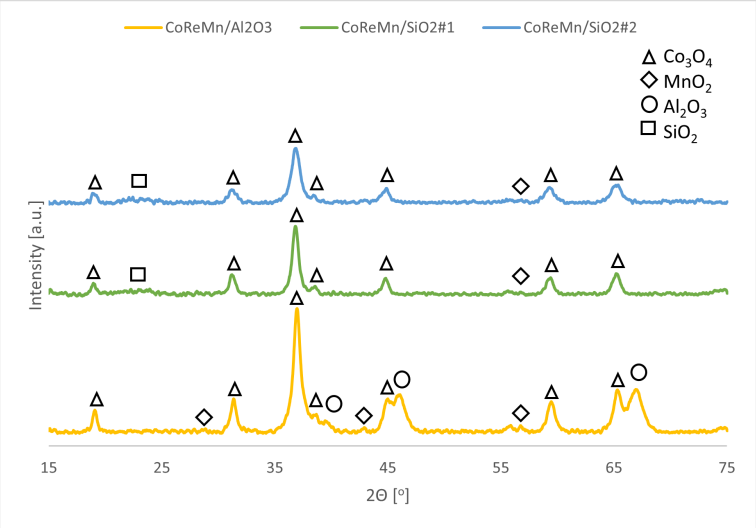

Figure 4.3: XRD patters with identified elements for the three cobalt based catalysts with Al_2O_3, SiO_2#1 and SiO_2#2 as support material

All FT experiments lasted for ~30 hours, where the first 24 hours detected the catalyst activity, and the last 6 hours were used to obtain selectivity measurements. The selectivity was measured at 50% CO conversion. The syngas feed flow was reduced to achieve higher CO conversions.

The activity results from the FT synthesis of the three catalysts are displayed below as CO conversion and site time yield (STY). In Figure 4.4 the CO conversion is highest at about 51% for the alumina-supported catalyst, which also obtains the best stability throughout the 24-hour long experiment. Silica#2 has a higher initial CO conversion at 4 hours, but the stability decreases to a value of 47% at 12 hours on stream. Silica#1 have the lowest CO conversion out of the three at 27% at 12 hours on stream. It can be speculated that a possible explanation for the reduced activity in the silica#1 supported catalyst is the possibility of sodium being present in the support from manufacturing. Sodium can be present in silica that is synthesized by precipitation where the starting materials contain sodium. Sodium is reported [80] to decrease the catalyst activity and can shift the product selectivity towards more C_{5+} and less CH_4.

Both silica#1 and silica#2 display lower stability than alumina with a decreasing factor of 0.4 and 0.5 per hour, respectively. Catalyst deactivation with time on stream may be due to sintering, surface cobalt oxidation, or solid-state reactions rendering inactive cobalt. As suggested from the dispersion and TPR results, alumina seems to have stronger metal-support interaction than silica, making the cobalt less prone to deactivation.

Figure 4.5 show the STY results for the three catalysts. Alumina again displays the best stability, but despite silica#2 having lower stability, the STY maintains at a higher value than alumina, even with alumina having higher dispersion than silica#2 as represented in Table 4.4. Again, silica#1 displayed the lowest activity measures for the FT synthesis reaction.

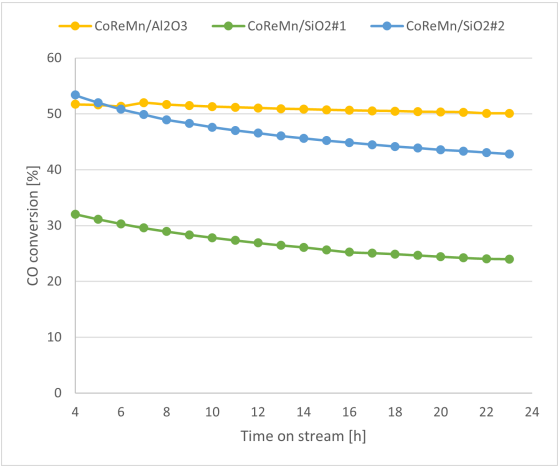

Figure 4.4: CO conversion plotted against time on stream (h) for the different supported cobalt catalysts (Al_2O_3, SiO_2#1 and SiO_2#2). Syngas feed flow was 250 ml/min, temperature was 240°C and pressure 5 bar.

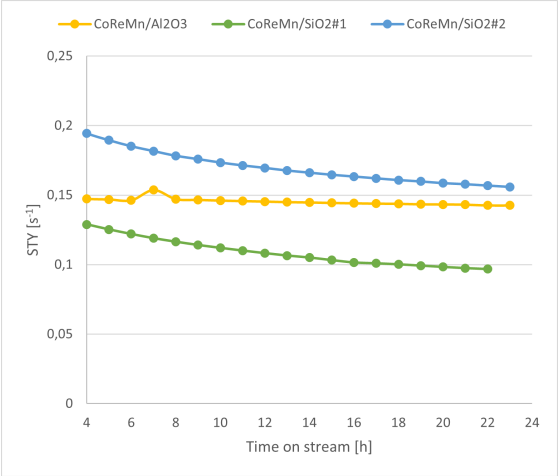

Figure 4.5: Site time yield (STY) plotted against time on stream (h) for the different supported cobalt catalysts (Al_2O_3, SiO_2#1 and SiO_2#2). Number of Co surface sited was determined by H_2-chemisorption. Syngas feed flow was 250 ml/min, temperature was 240°C and pressure 5 bar.

As mentioned before, the selectivity data were measured at 50% CO conversion for all catalysts. Figure 4.6 show the carbon selectivity product distribution results of the FT synthesis of the three different supported catalysts. The product distribution is divided into CO_2, CH_4, C_{2-4} alpha-olefins, C_{2-4} iso-olefins, C_{2-4} paraffins, and the rest of the products as C_{5+}. Silica#1 displays the highest selectivity towards C_{5+} and lowest towards CH_4, which can support the statement that this silica support material contains fractions of sodium from manufacturing, where sodium if proven to shift selectivity in such manner [80]. All catalysts displayed low selectivity towards the production of CO_2.

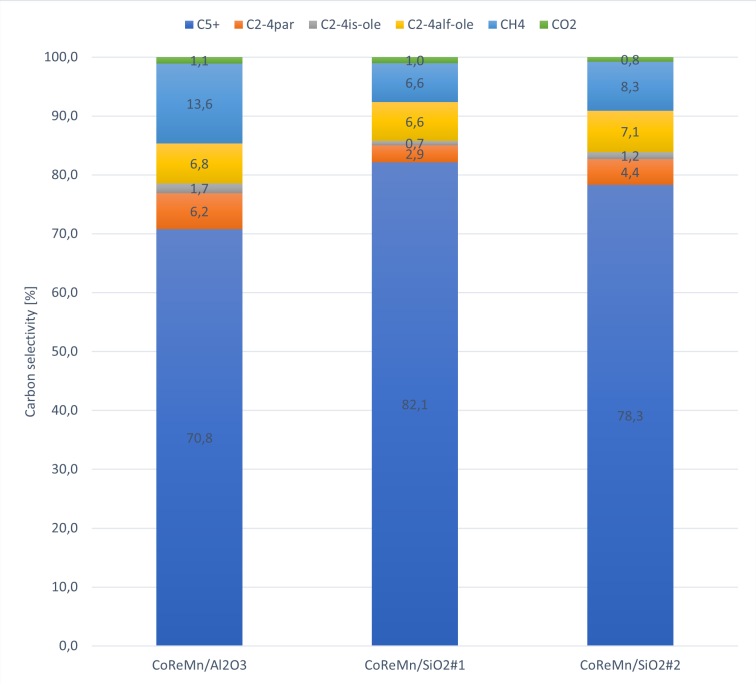

Figure 4.6: Carbon product selectivity at 50% CO conversion and ~27 h time on stream for the differnt supported catalysts. Feed flow of syngas was adjusted to reach 50% CO conversion. Temperature and pressure were 240°C and 5 bar, respectively.

Figure 4.7 show that the C_{5+} selectivity increases in the following order: Al_2O_3 < SiO_2#2 < SiO_2#1. This is the same order as the pore volume seen in Table 4.3. The metal particle size measured by H_2-chemisorption (Table 4.4) also follows the same trend. It has previously been reported that C_{5+} selectivity increases when cobalt is supported by materials with a low surface area instead of a high surface area [80]. This does not correspond with the present results where alumina has the lowest surface area out of the three support materials, but not the highest C_{5+} selectivity. However, when comparing the two silica supports, silica#1 with a lower surface area than silica#2 does display a higher C_{5+} selectivity. It was also reported that pore size influences the chain growth probability where larger pores have a higher probability of producing longer chained hydrocarbons [80]. In the case of the present results, this would mean that alumina with the highest measured pore size would display the highest C_{5+} selectivity, which it does not. However, when comparing the two different silica-supported catalysts, the statement seems to be accurate. This indicates that there are factors other than the structural characteristics of the supports that originate from the difference in product selectivity between alumina and silica as support materials.

In Figure 4.8 the same but opposite trend as for C_{5+} can be seen for the CH_4 selectivity, where silica#1 have the lowest CH_4 selectivity out of the three. This suggests that the increase in C_{5+} selectivity is a result of decreased CH_4 selectivity. Increased C_{5+} and decreased CH_4 selectivity indicates that a higher chain growth probability is present for the silica supported catalysts compared to the alumina supported catalyst [81].

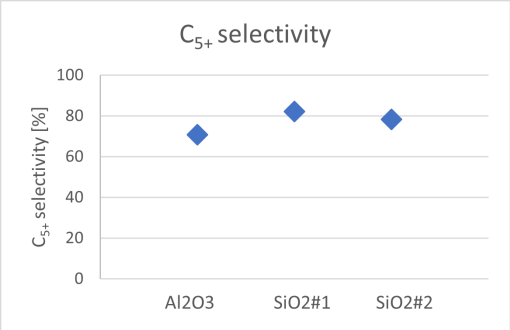

Figure 4.7: C_{5+} selectivity at 50% CO conversion and ∼27 h time on stream. Feed flow of syngas was adjusted to reach 50% CO conversion. Temperature and pressure were 240°C and 5 bar, respectively.

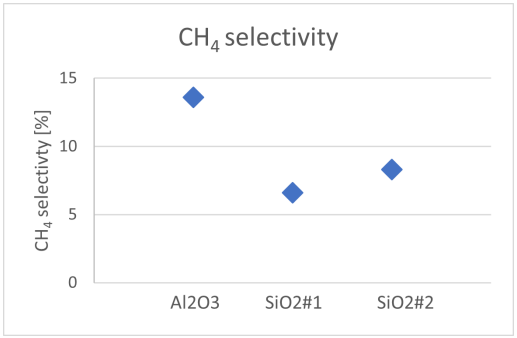

Figure 4.8: CH_4 selectivity at 50% CO conversion and ∼27 h time on stream. Feed flow of syngas was adjusted to reach 50% CO conversion. Temperature and pressure were 240°C and 5 bar, respectively.

Light α-olefins are the most desired product for the aim of this project. There is no significant difference between the support materials for the C_{2-4} α-olefin selectivity (Figure 4.9) even though there are changes in the selectivity towards the other products. This can indicate that the readsorption of olefins may be independent on the type of support material used. For the C_{2-4} paraffin selectivity (Figure 4.10), the silica-supported catalysts, especially silica#1, display lower selectivity. This may indicate that the support material influences the hydrogenation rate resulting in lower paraffin formation. It has previously been reported that smaller pore sizes can increase the possibility of secondary reactions of olefins due to transport limitations [80]. The pore size of silica#2 is half the size of the other support materials. The light α-olefin selectivity for silica#2 is not lower than the others, but the light paraffin selectivity is higher for silica#2 than silica#1. This indicates that the difference in pore sizes explored in this study may have an impact on selectivity to light paraffins. The hydrogenation activity of the different catalysts can be seen with the production of CH_4, paraffins and C_{5+}. An increase of CH_4 is attributed to a higher rate of termination by hydrogenation, and a increase in paraffin is attributed to higher rate of hydrogenation of the alkyl chain, decreasing then the C_{5+} selectivity by limiting the chain growth probability.

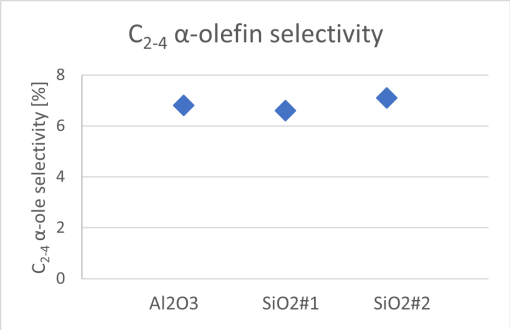

Figure 4.9: C_{2-4} α-olefin selectivity at 50% CO conversion and ~27 h time on stream. Feed flow of syngas was adjusted to reach 50% CO conversion. Temperature and pressure were 240°C and 5 bar, respectively.

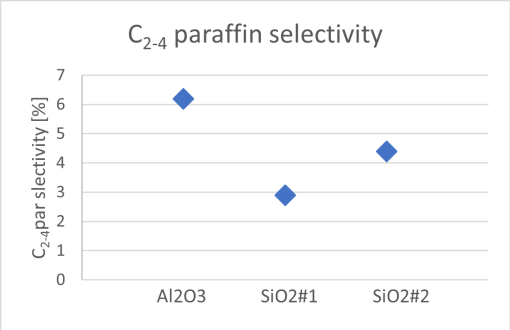

Figure 4.10: C_{2-4} paraffin selectivity at 50% CO conversion and ~27 h time on stream. Feed flow of syngas was adjusted to reach 50% CO conversion. Temperature and pressure were 240°C and 5 bar, respectively.

The α-olefin/paraffin ratio for product selectivity of the three catalysts is shown in Figure 4.11. The silica#1 supported catalyst displays the highest ratio, while the alumina-supported catalyst has the lowest ratio out of the three. The increase in α-olefin selectivity is lessened by the shift towards heavier products and is highest for C_3 products for all catalysts.

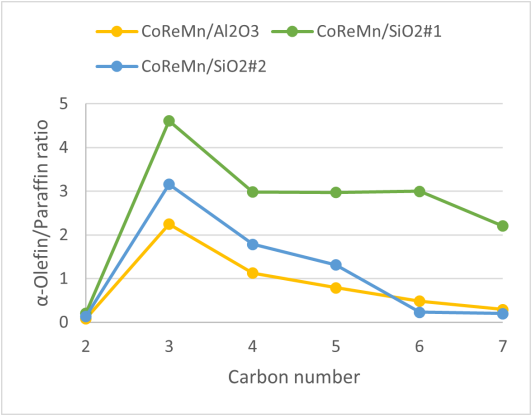

Figure 4.11: α-olefin/paraffin ratio as a function of carbon number obtained at 50% CO conversion and ~ 27 h time on stream. Feed flow of syngas was adjusted to reach 50% CO conversion. Temperature and pressure were 240°C and 5 bar, respectively.

The results indicate that alumina display higher metal-support interactions than silica, making it less prone to deactivation [82]. Silica supported catalysts display lower selectivity towards CH_4 and light paraffins, while the selectivity towards light olefins is approximately the same regardless of the three support materials used. Silica-supported catalysts obtained higher α-olefin/paraffin ratios than the alumina-supported catalyst, suggesting that silica can be the more suitable support material when a higher yield of light olefin production is desired.

4.2 Promoting Effect of Manganese

The promoting effect of manganese was investigates using the silica#2 type of silica support material. Four catalysts are involved for the evaluation of manganese promotion: the reference catalyst $CoRe/SiO_2$, the standard catalyst with 3.75 wt% Mn, and the two catalysts with different Mn composition of 1.5wt% and 5wt%.

Surface area, pore volume and pore size obtain from BET and BJH method for the four catalysts can be seen in Table 4.5. No changes can be seen in the pore volume and pore size, which indicates that there is an even distribution of the Mn in the pores. The small deviations can be ruled out as measurement errors. There is a minor increase in surface area for 1.5%Mn and a decrease for 5%Mn compared to the reference catalyst, but again this can be considered as measurements errors as they differ 5% or less. This suggests that addition of Mn have little effect on such characteristics of the catalyst.

Table 4.5: Results of surface area, pore volume and pore size obtained by the BET and BJH method for the catalysts with differing amounts of Mn loadings.

Catalyst	**Surface area** [m^2/g]	**Pore volume** [cm^3/g]	**Pore size** [**nm**]
$CoRe/SiO_2$	388	0.53	4.5
1.5%Mn-$CoReMn/SiO_2$	405	0.54	4.4
$CoReMn/SiO_2$	389	0.52	4.4
5%Mn-$CoReMn/SiO_2$	368	0.49	4.4

The results from H_2-chemisorption including dispersion and metal particle size is presented in Table 4.6, as well as the results from XRD including the crystallite size and dispersion. For the H_2-chemisorption measured dispersion, significant differences are observed ranging from 6.6 to 9.6%. The standard catalyst with 3.75wt% Mn had the lowest measured dispersion, while the catalyst with 1.5wt% Mn had the highest dispersion. There does not appear to be a trend between Mn loading and measured Co dispersion as the 5%Mn catalyst with the highest Mn loading does not have the lowest dispersion. The results from XRD however, display a trend of reduced cobalt crystallite size and increased dispersion with increased Mn loading. Blockage of Co sited by Mn could be a possible explanation for the reduced dispersion. This does not however, explain why the 5%Mn with the highest Mn loading display higher dispersion than the standard catalyst with lower loading. The catalyst with 1.5wt% Mn could have sufficiently low enough Mn loading to not block any important Co sites, resulting in no reduction of dispersion. It has been reported that small amounts of Mn may have a beneficial effect on dispersion[58]. This was attributed to Mn forming a mixed compound with the support and inhibiting strong metal-support interactions with Co. Increasing the amount of Mn resulted in a lowered dispersion agreeing with the present results. Mn can also form mixed oxides with Co[78;79] which can reduce the amount of available

active Co metal, thus reducing the dispersion obtained by H_2-chemisorption. The possibility of mixed oxide formation with excess Mn can be an explanation of the reduced dispersion obtained for the catalysts with higher Mn loadings (3.75 and 5wt%).

Table 4.6: Characterization results for the catalysts with differing amount of Mn loadings. The results include cobalt dispersion (D_{chem}) and metal particle size (M_{ps}) obtained from H_2-chemisorption, and cobalt dispersion (D_{XRD}) and crystallite size (τ_{Co}) obtained from XRD.

Catalyst	**H_2-chemisorption**		**XRD**	
	D_{chem} [%]	**M_{ps} [nm]**	**D_{XRD} [%]**	**τ_{Co} [nm]**
$CoRe/SiO_2$	9.3	10.3	10.7	9.0
1.5%Mn-$CoReMn/SiO_2$	9.6	10.0	12.1	8.0
$CoReMn/SiO_2$	6.6	14.5	12.3	7.8
5%Mn-$CoReMn/SiO_2$	7.5	12.9	12.9	7.4

Figure 4.12 show the TPR profiles of the four catalysts. A maximum of four peaks were observed during the experiments. The first peak, which is most prominent in the standard catalyst and the 5%Mn catalyst, can be attributed to the reduction of nitrate remaining after calcination [76;44]. The second peak is similar for all four catalysts and represents the reduction of Co_3O_4 to CoO [83]. The third peak, most prominent in 1.5%Mn, originate from the second reduction step from CoO to Co [83]. The fourth peak is suggested to be a delayed reduction of CoO, possibly with simultaneous reduction of Mn, or a $Co_{3-X}Mn_XO_4$ type mixed oxide which is reportedly formed by CoMn catalysts [78;79]. There is a slight correlation between higher Mn loadings and lower reduction temperature which has been reported in previous studies [79;54]. This suggests that Mn may improve the reducibility of the catalyst.

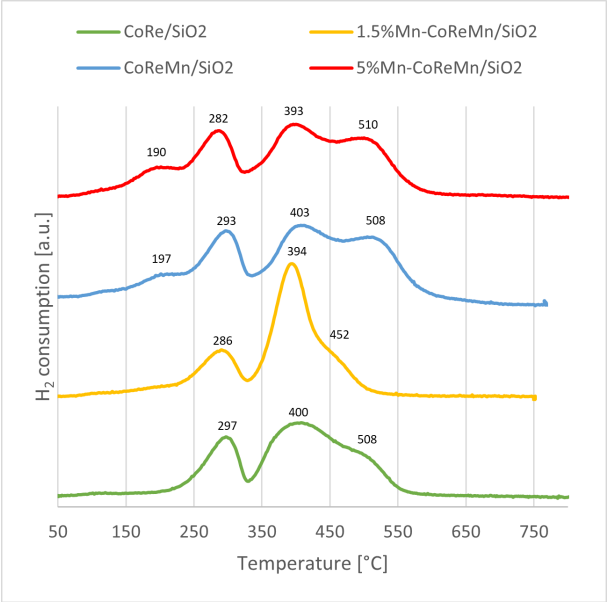

Figure 4.12: TPR profile as H_2 consumption as a function of the bed temperature for the catalysts with differing amounts of Mn loadings. The reaction conditions were 50 mL/min of 10%H_2/Ar flow and 800°C (10°C/min).

The XRD profiles for the catalysts are displayed in Figure 4.13, including a sample of SiO_2 impregnated with 3.75wt% Mn. Observing the XRD patterns, a weak MnO_2 signal is visible at 37 and 57°. This is most apparent for the sample with only Mn on SiO_2. The first MnO_2 peak falls under the highest Co_3O_4 signal for the other samples, and the last MnO_2 becomes less apparent with cobalt present in the sample. This suggests that Mn may be to a larger extent incorporated in the Co_3O_4 particles, possibly forming Co-Mn mixed oxides.

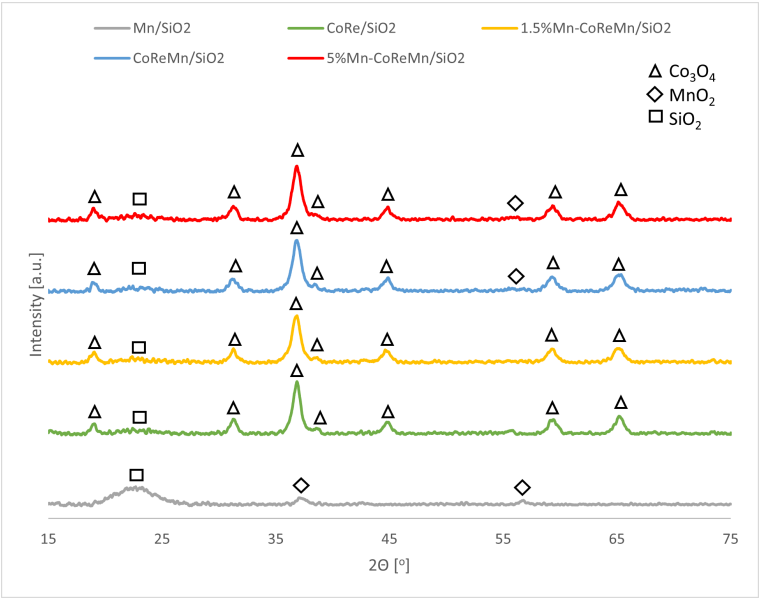

Figure 4.13: XRD patters with identified elements for the catalysts with differing amounts of Mn loadings (0-5 wt%).

The CO conversion and STY for the catalysts in the initial 24 h of operation are shown in Figure 4.14 and Figure 4.15, respectively. Observing the intrinsic activity in Figure 4.15, it can be seen that all Mn-promoted catalysts exhibit STY slightly higher than the unpromoted reference catalyst. The unpromoted catalyst however, display less deactivation during the 24 h on stream compared to the promoted catalysts.

The catalyst performance is approximately 47% CO conversion at 12 h on stream for all catalysts except the 1.5%Mn catalyst which displayed a CO conversion of 61%. *Dinse et al.*[53] studied the effect of Mn/Co ratio with SiO_2 support at 1 bar, and found that the CO consumption increased for Mn/Co ratios up to 0.05 and decreased again for higher Mn loadings. These results are coherent with the results obtained in this study where the 1.5%Mn catalyst with a Mn/Co loading of 0.1 displayed the highest conversion activity. The process condition of 5 bar used in this study could possibly have shifted the threshold value of Mn/Co ratio found by Dinse et al. A study by *Johnson et al.*[84] reported an increased rate of CO consumption and CO adsorption by Mn promotion, where the Mn increased the abundance of adsorbed CO with weakened the C-O bonds. It was proposed that the weakening of the C-O bond is promoted though Lewis acid-base interactions between Mn^{2+} cations located at the edge of the MnO covering the Co particles, and that the O atom of CO adsorbates to the MnO. Weak CO bonds might lead to higher carbon formation, which could explain the higher stability of the unpromoted reference catalyst. It was further found by *Johnson et al.*[84;85] that for Mn/Co ratios above 0.1, excess Mn decorates the SiO_2 surface as MnO spectator species. The Mn-promoted catalysts of this study have Mn/Co ratios of 0.1, 0.25 and 0.33, where the two latter are above the threshold value found by Johnson et al. An excess of Mn may explain the similar behaviour in CO conversion of the catalysts with higher Mn loading.

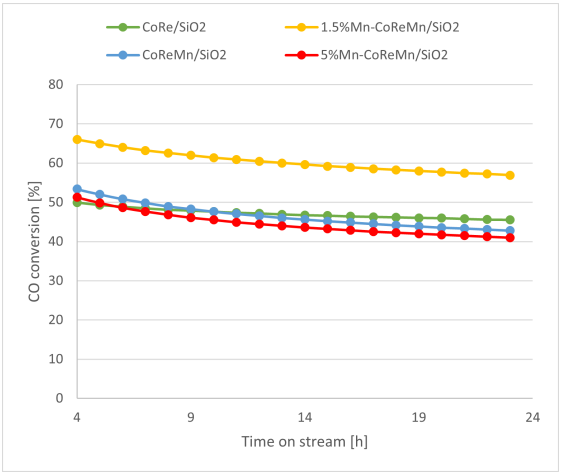

Figure 4.14: CO conversion plotted against time on stream (h) for catalyst with different Mn loadings from 0 to 5wt%. Syngas feed flow was 250 ml/min, temperature was 240°C and pressure 5 bar.

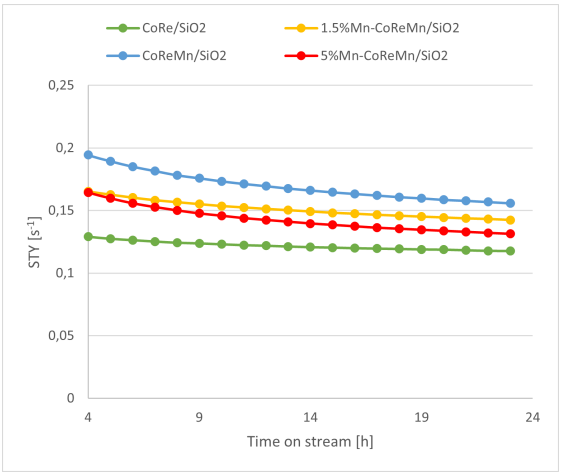

Figure 4.15: Site time yield (STY) plotted against time on stream (h) for catalyst with different Mn loadings from 0 to 5wt%. Number of Co surface sited was determined by H_2-chemisorption. Syngas feed flow was 250 ml/min, temperature was 240°C and pressure 5 bar.

Figure 4.16 show the carbon product selectivity results of the four catalysts. There appear to be an increase in C_{5+} and decrease in CH_4 selectivity with Mn promotion. It is also an increase in C_{2-4} olefin selectivity and decrease is C_{2-4} paraffin selectivity with Mn present. All catalysts displayed low selectivity towards CO_2 and C_{2-4} iso-olefins.

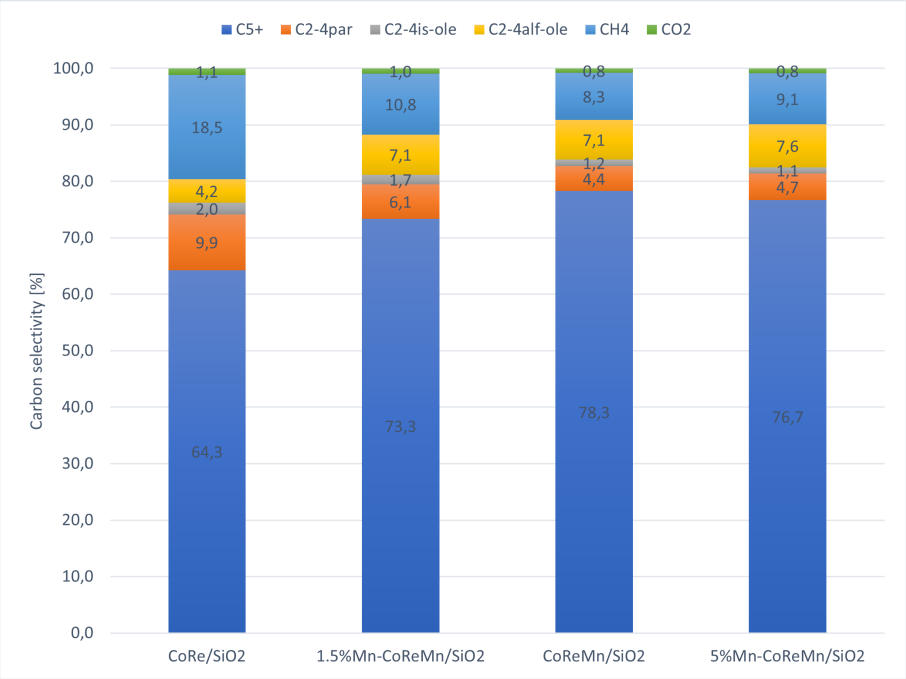

Figure 4.16: Carbon product selectivity at 50% CO conversion and ~27 h time on stream. Feed flow of syngas was adjusted to reach 50% CO conversion. Temperature and pressure were 240°C and 5 bar, respectively.

Figure 4.17 show the C_{5+} selectivity results of the catalysts with Mn loadings from 0 to 5wt%. The results suggest that Mn promotion increases the C_{5+} selectivity until 3.75wt% Mn, and decreases again with 5wt% Mn. The same but opposite trend is shown in Figure 4.18 where the CH_4 selectivity decreases until 3.75wt% Mn and increases again with 5wt% Mn. This indicates that there may be a maximum point of Mn loading where the promoting effect on selectivity reverses itself with respect to C_{5+} and CH_4 production. The decrease in selectivity to CH_4 and increased selectivity to C_{5+} products with increasing Mn/Co ratio are suggested to be attributed to a decrease in the ratio of adsorbed H to CO on the surface of the Mn support cobalt particles [84].

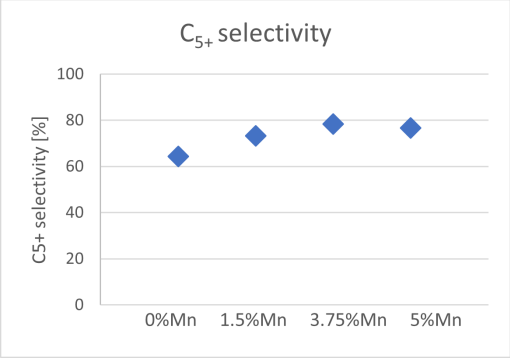

Figure 4.17: C_{5+} selectivity at 50% CO conversion and ~27 h time on stream. Feed flow of syngas was adjusted to reach 50% CO conversion. Temperature and pressure were 240°C and 5 bar, respectively.

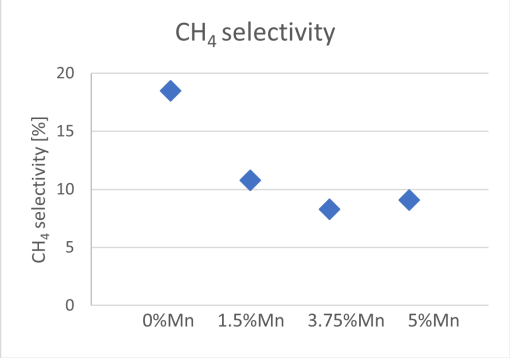

Figure 4.18: CH_4 selectivity at 50% CO conversion and ~27 h time on stream. Feed flow of syngas was adjusted to reach 50% CO conversion. Temperature and pressure were 240°C and 5 bar, respectively.

Figure 4.19 show the difference in C_{2-4} α- olefin selectivity for the catalysts with Mn loadings from 0 to 5wt%. The light olefin selectivity is notably higher for the Mn-promoted catalysts than the unpromoted catalyst, and it appears to increase with increased Mn loading. An opposite trend is seen in Figure 4.20 for the C_{2-4} paraffin selectivity where it decreases with increasing Mn loading until 3.75wt%. This suggests that Mn promotes the product termination to α-olefins, and possibly reduced selectivity towards hydrogenation reactions. This was also found in previous studies [52;25;53].

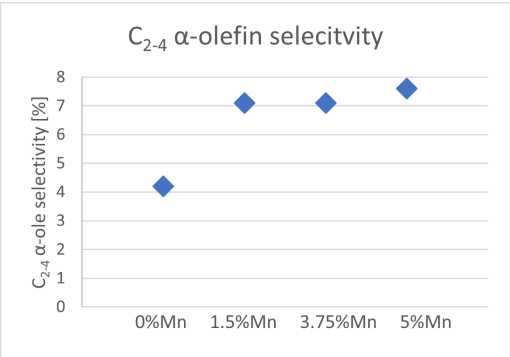

Figure 4.19: C_{2-4} α-olefin selectivity at 50% CO conversion and ~27 h time on stream. Feed flow of syngas was adjusted to reach 50% CO conversion. Temperature and pressure were 240°C and 5 bar, respectively.

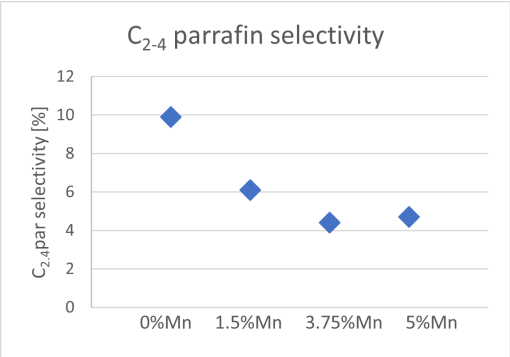

Figure 4.20: C_{2-4} paraffin selectivity at 50% CO conversion and ~27 h time on stream. Feed flow of syngas was adjusted to reach 50% CO conversion. Temperature and pressure were 240°C and 5 bar, respectively.

The α-olefin/paraffin ratio for the different catalysts at 50% CO conversion is shown in Figure 4.21. The two highest Mn loaded catalysts siplay the highest ratio, supporting the suggestion that Mn promotes olefin selectivity. The increase in α-olefin selectivty is lessened by the shift towards heavier products and is highest for C_3 products.

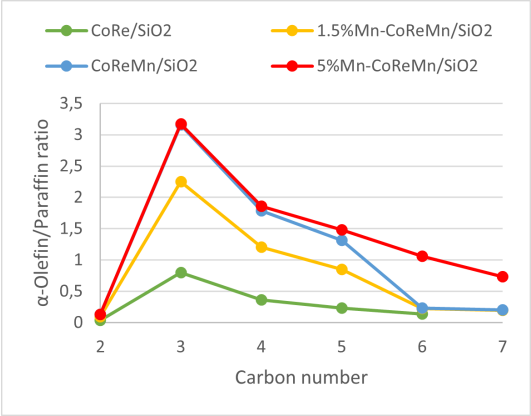

Figure 4.21: α-olefin/paraffin ratio as a function of carbon number at 50% CO conversion and ~27 h time on stream. Feed flow of syngas was adjusted to reach 50% CO conversion. Temperature and pressure were 240°C and 5 bar, respectively.

The results of these experiments show that for silica-supported cobalt catalysts, Mn-promotions shifts the product selectivity towards more light olefins and C_{5+}, and less light paraffins and CH_4. The results also suggests that a Mn/Co ratio of 0.1 may be a optimal ratio for increasing CO conversion by Mn promotion. It is also suggested that higher Mn/Co ratios results in an excess of Mn which may be present as MnO spectator species on the support. Interestingly, the increased activity with a low Mn/Co ratio does not correlate with the difference in selectivity, which could mean that the mechanism for the increased activity and the changes in selectivity by manganese promotion is of different nature.

4.3 The Effect of Phosphorous Contamination

As mentioned, phosphorous (P) is an impurity that may be present in the syngas feed to the FT synthesis, especially for biomass-derived syngas. To simulate such impurity pick-up by the catalyst, a P precursor was impregnated with the standard catalyst ($CoReMn/SiO_2$) in two different concentrations, 1700 ppmw (P1) and 6700 ppmw (P2). The effect of phosphorous was tested on both the silica#1 and silica#2 type supported catalysts. In total, four P-containing catalysts were prepared: P1-$CoReMn/SiO_2$#1, P2-$CoReMn/SiO_2$#1, P1-$CoReMn/SiO_2$#2, and P2-$CoReMn/SiO_2$#2. The catalysts containing P are compared to their original standard catalyst.

Table 4.7 show the results of surface area, pore volume and pore size obtained by the BET and BJH methods. No significant changes can be seen in the pore volume and average pore size after P-impregnation. However, there is a trend in reduced BET surface area after P-impregnation, which can be due to pore blockage. When pore blockage occurs, there is expected to be a change in pore size but the average pore size does is not changed in these results. A slight decrease in pore volume is observed for the silica#1 supported catalysts after P-impregnation, suggesting P is placed inside the pores with the Co. However, the change is very small and therefore it can be assume that the pores are not physically blocked by the P and that the Co particles are available.

Table 4.7: Results of surface area, pore volume and pore size obtained by the BET and BJH method for the differnt silica supported catalysts with varying amounts of P compared to its standard catalyst.

Catalyst	**Surface area** [m^2/g]	**Pore volume** [cm^3/g]	**Pore size** [**nm**]
$CoReMn/SiO_2$#1	236	0.82	11.8
P1-$CoReMn/SiO_2$#1	224	0.77	11.8
P2-$CoReMn/SiO_2$#1	217	0.77	11.8
$CoReMn/SiO_2$#2	389	0.52	4.4
P1-$CoReMn/SiO_2$#2	375	0.51	4.4
P2-$CoReMn/SiO_2$#2	366	0.51	4.5

The results obtained by H_2-chemisorpstion for cobalt dispersion and metal particle size is shown in Table 4.8, and display reductions in dispersion and metal particle size after P-impregnation. The changes in H_2-chemisorption metal particle size are based on the obtained dispersion. For both silica#1 and silica#2, impregnation of P reduced the dispersion, which gives an indicates that the FT activity can be expected to be reduced. The decrease in dispersion and increase in particle size based on H_2-chemisorption might be due to sintering of the cobalt particles or by P blocking cobalt active sites. Table 4.8 also show the results obtained by XRD for the cobalt crystallite size and dispersion, which does not display any major changes as seen in the H_2-chemsorption results. This decrease in dispersion by H_2-chemisorption but not in XRD could mean that there is no increase in particle size and that the P is inhibiting the hydrogen chemisorption leading to an underestimation

of the metallic dispersion. The trend of P2 for decreased dispersion is not the same for the two different silica-supported catalysts, but this may be due to experimental error as the Langmuir isotherm of P2-CoReMn/SiO_2#2 did not appear as an expected Langmuir isotherm. A couple of the obtained Langmuir isotherms can be found in Appendix B.

Table 4.8: Characterization results for the different silica supported catalysts with varying amounts of P compared with the standard catalysts. The results include cobalt dispersion (D_{chem}) and metal particle size (M_{ps}) obtained from H_2-chemisorption, and cobalt dispersion (D_{XRD}) and crystallite size (τ_{Co}) obtained from XRD.

Catalyst	**H_2-chemisorption**		**XRD**	
	D_{chem} [%]	**M_{ps} [nm]**	**D_{XRD} [%]**	**τ_{Co} [nm]**
CoReMn/SiO_2#1	6.0	16.0	9.3	10.4
P1-CoReMn/SiO_2#1	4.0	24.1	8.8	10.9
P2-CoReMn/SiO_2#1	2.7	36.1	8.8	10.9
CoReMn/SiO_2#2	6.6	14.5	12.3	7.8
P1-CoReMn/SiO_2#2	4.6	20.9	12.5	7.7
P2-CoReMn/SiO_2#2	4.7	20.5	12.1	8.8

P did not contribute to any change in the XRD profile plots. The XRD profile plots of the catalysts can be found in Appendix B.

Figure 4.22 and Figure 4.23 show the TPR profiles of the six catalysts. As described in the previous chapters, the first small peak can be attributed to the reduction of nitrate remaining after calcination [76;44]. The second peak represents the reduction of Co_3O_4 to CoO [83]. The third peak originates from the second reduction step from CoO to Co [83]. The fourth peak is suggested to be a delayed reduction of CoO, possibly with simultaneous reduction of Mn, or a $Co_{3-X}Mn_XO_4$ type mixed oxide [78;79]. A trend of increased reduction temperatures (20-40℃) with increased P loading can be seen for both silica-supported catalysts. This suggest that more strongly interacting Co species are present when P is added. The change in reduction temperature indicates that the reducibility of the catalyst is decreased. This is an undesired effect as it can contribute to less of the oxidized cobalt being reduced to its active metallic state for the FT synthesis.

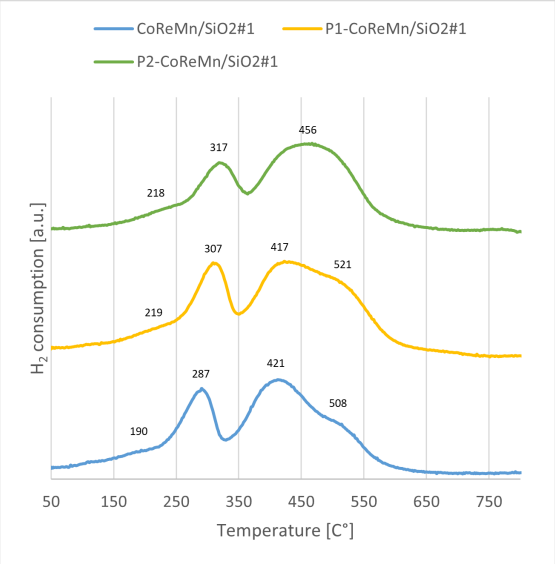

Figure 4.22: TPR profile of the standard SiO_2#1 supported catalyst compared to the catalysts with 1700 (P1) and 6700 ppmw (P2) phosphorous contamination. The reaction conditions were 50 mL/min of 10%H_2/Ar flow and 800°C (10°C/min).

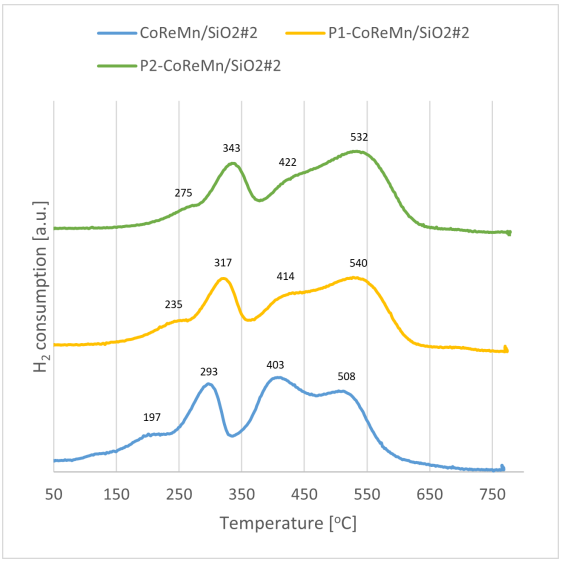

Figure 4.23: TPR profile of the standard SiO_2#2 supported catalyst compared to the catalysts with 1700 (P1) and 6700 ppmw (P2) phosphorous contamination. The reaction conditions were 50 mL/min of 10%H_2/Ar flow and 800°C (10°C/min).

As expected by the Co dispersions found in Table 4.6, the presence of P in the catalysts decreased the FT activity. Figure 4.24 and Figure 4.25 show the results of the FT experiments for CO conversion (%) and STY (s^{-1}), respectively. For silica#1, P1 lead to a 71% reduction in CO conversion, while P2 caused a 95% reduction, almost completely deactivating the catalyst. Similarly, for silica#1, P1 and P2 reduced the CO conversion by 65 and 91%. The STY data is dependent on Co dispersion and the reaction rate of CO conversion, thus the results follow the same trend as these factors. There may be several reasons why the activity decreased with the presence of P. Physical blocking of active Co sites is one possibility [86]. For this to be the case, one P atom must block several Co atoms due to the quantity difference of 0.17 and 0.67wt% P versus 15wt% Co which corresponds to only 1.1 and 4.5% blockage of Co atoms. Electronic effects are another possibility for reduced activity. P is more electronegative than Co. The bond strength between CO and metal strongly depends on the electron back-donation from metal to CO [85]. Promoters or other species present on the catalyst with relative high electronegativity acts as electron-accepting species weakening the CO adsorption resulting in a lower adsorbed CO/H ratio on the Co surface. This could shift the coverage of CO and H_2 reducing its activity. The exact mechanism responsible for the deactivation of P is not clear.

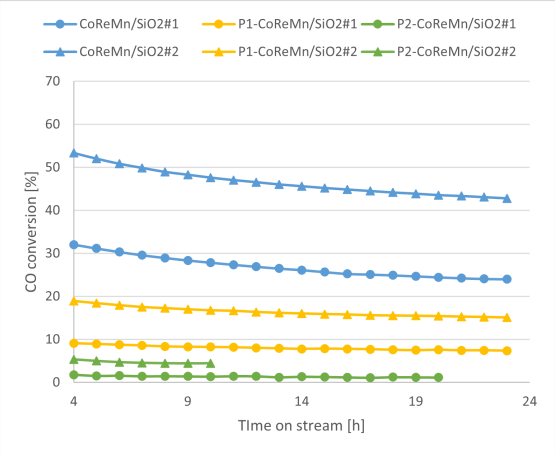

Figure 4.24: CO conversion plotted against time on stream (h) for the standard silica-supported catalysts and the corresponding catalysts with 1700 (P1) and 6700ppmw (P2) phosphorous loadings. Syngas feed flow was 250 ml/min, temperature was 240°C and pressure 5 bar.

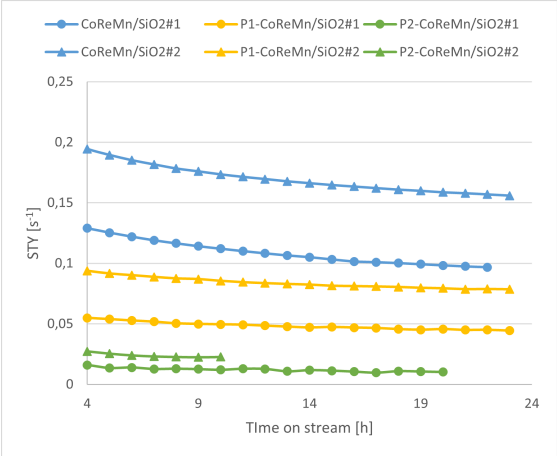

Figure 4.25: Site time yield (STY) plotted against time on stream (h) for the standard silica-supported catalysts and the corresponding catalysts with 1700 (P1) and 6700ppmw (P2) phosphorous loadings. Number of Co surface sited was determined by H_2-chemisorption. Syngas feed flow was 250 ml/min, temperature was 240°C and pressure 5 bar.

As described earlier, all selectivity measurements were to be executed at 50% CO conversion to compare the different catalyst performances. To increase CO conversion, the feed of syngas must be reduced. As the activity for the two P2 catalysts was significantly low, the calculated space velocity of syngas to theoretically reach 50% conversion was too low for the system to operate at. Hence, selectivity measurements for the P2 catalysts were not obtained. Figure 4.6 show the carbon product selectivity of the P1 catalysts compared to the standard catalysts. There is an increase in the product selectivity to CO_2 and C_{2-4} iso-olefins for the catalysts with 1700 ppmw P. There also seems to be a correlation between a reduction in C_{5+} selectivity and an increase in CH_4 selectivity. This is an unwanted selectivity change as CH_4 is the least desired product of the FT synthesis.

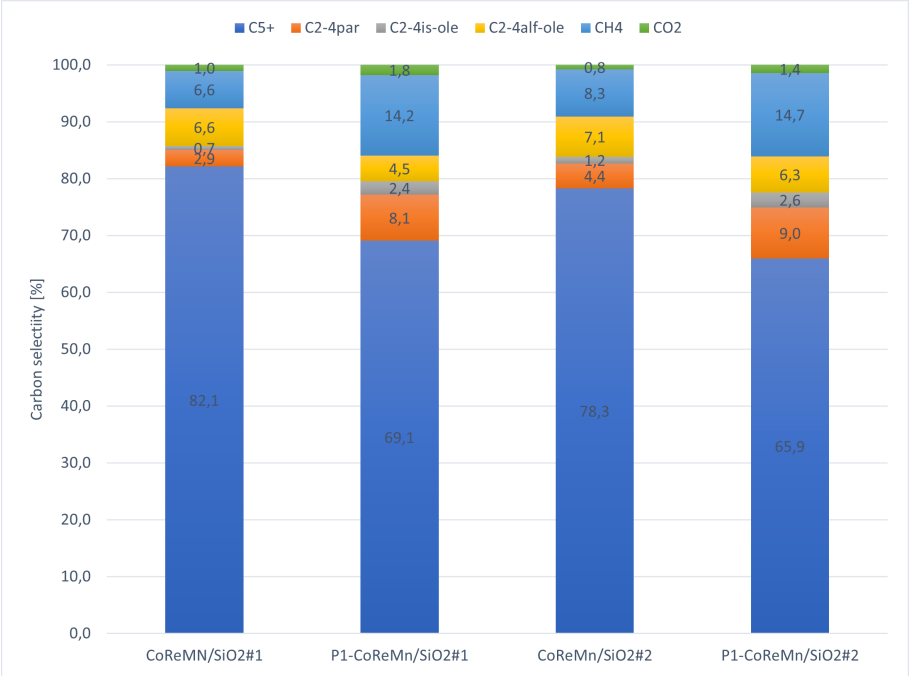

Figure 4.26: Carbon product selectivity at 50% CO conversion and ∼27 h time on stream. Feed flow of syngas was adjusted to reach 50% CO conversion. Temperature and pressure were 240°C and 5 bar, respectively.

Figure 4.27 and Figure 4.28 show the selectivity change in C_{5+} and CH_4 selectivity after addition of 1700 ppmw P to the catalysts. The selectivity to C_{5+} increases, while the selectivity to CH_4 decreases for both types of silica-supported catalysts. It has previously been reported that P inhibits hydrogen desorption, yielding higher hydrogen to carbon ratios during reaction [86]. This would favor chain termination, resulting in the trend observed here of higher CH_4 and lower C_{5+} product selectivity.

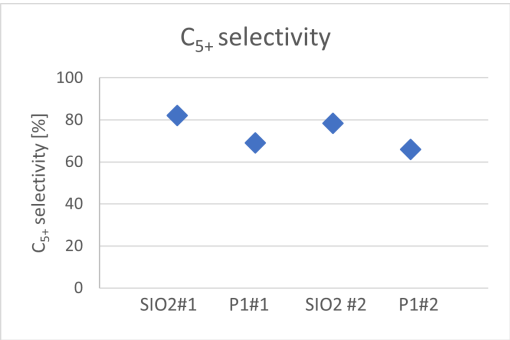

Figure 4.27: C_{5+} selectivity at 50% CO conversion and ∼27 h time on stream. Feed flow of syngas was adjusted to reach 50% CO conversion. Temperature and pressure were 240°C and 5 bar, respectively.

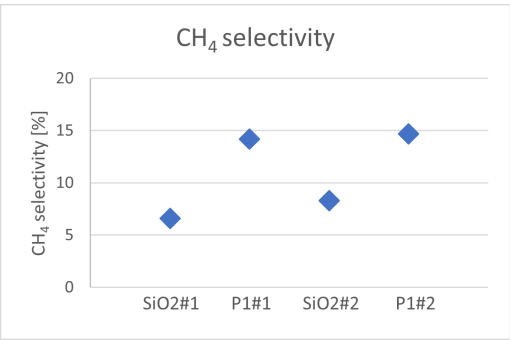

Figure 4.28: CH_4 selectivity at 50% CO conversion and ∼27 h time on stream. Feed flow of syngas was adjusted to reach 50% CO conversion. Temperature and pressure were 240°C and 5 bar, respectively.

The change in C_{2-4} α-olefin selectivity and C_{2-4} paraffin selectivity are shown in Figure 4.29 and Figure 4.30, respectively. P appears to decrease the light α-olefin selectivity, while also increasing

the light paraffin selectivity. This can indicate that P increases the termination rate by hydrogenation to paraffins, and reduces the termination rate to olefins. The reduced α-olefin/paraffin ratio by P can also be seen in Figure 4.31.

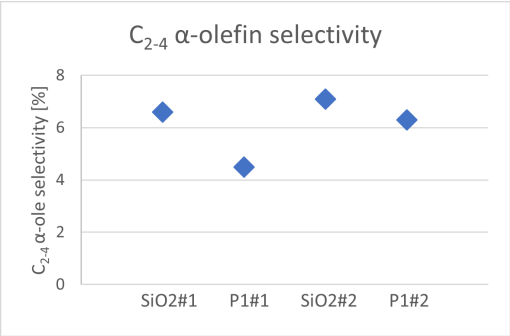

Figure 4.29: C_{2-4} α-olefin selectivity at 50% CO conversion and ~27 h time on stream. Feed flow of syngas was adjusted to reach 50% CO conversion. Temperature and pressure were 240°C and 5 bar, respectively.

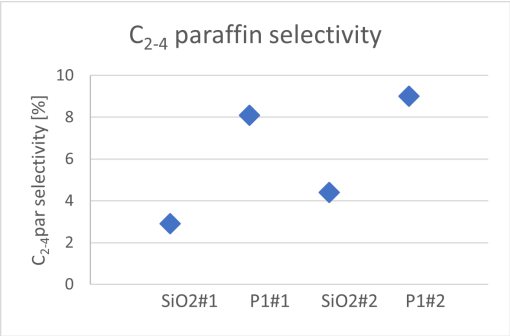

Figure 4.30: C_{2-4}Paraffin selectivity at 50% CO conversion and ~27 h time on stream. Feed flow of syngas was adjusted to reach 50% CO conversion. Temperature and pressure were 240°C and 5 bar, respectively.

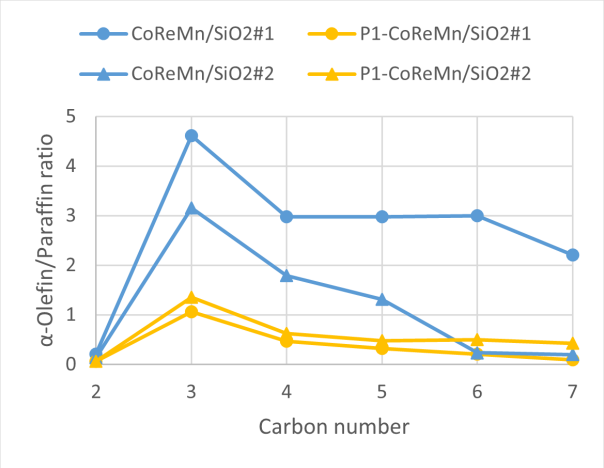

Figure 4.31: α-olefin/paraffin ratio as a function of carbon number obtained at 50% CO conversion and ~ 27 h time on stream. Feed flow of syngas was adjusted to reach 50% CO conversion. Temperature and pressure were 240°C and 5 bar, respectively.

The results clearly show that phosphorous decreases activity for silica-supported cobalt catalysts and negatively impacts the product selectivity, and should therefore be avoided in all steps of FT catalyst synthesis and application.

5 Conclusion and Future Work

5.1 Conclusion

Cobalt-based catalysts have been studied for the Fischer-Tropsch synthesis in terms of support material, manganese promotion, and phosphorous contamination.

It was suggested that γ-Al_2O_3 have higher metal-support interactions than SiO_2, resulting in higher metal dispersion and catalyst stability. The SiO_2-supported catalysts had higher olefin/paraffin ratios than the γ-Al_2O_3-supported catalysts, indicating that SiO_2 hinders the rate of hydrogenation reactions generating paraffins.

SiO_2-supported cobalt catalysts were impregnated with 0, 1.5, 3.75, and 5 wt% manganese. The results indicated that light olefin product selectivity increased with increased manganese promotion. It was also suggested that an Mn/Co ratio of 0.1 increases the CO conversion of the catalyst.

Phosphorous contamination was simulated by impregnating 1700 and 6700 ppmw phosphorous to SiO_2-supported catalysts. The experimental results showed that phosphorous significantly decreased the catalyst activity, negatively changing the properties of the cobalt.

5.2 Suggestions for Future Work

As the γ-Al_2O_3-supported catalyst displayed higher stability than the SiO_2-supported catalysts, it would be interesting to test it for phosphorous contamination to see if the γ-Al_2O_3 can improve the catalyst's tolerance for contamination.

Catalyst preparation and testing for the catalyst with Mn/Co ratio 0.1 should be repeated to confirm the results obtained in this study. Further investigation is needed to find out why this ratio causes higher CO conversion than higher Mn/Co ratios.

Further work should be done to identify the mechanisms taking place for the catalyst deactivation by phosphorous contamination. It may also be desired to find a safe way to introduce the impurity in the syngas flow as it would be a more accurate representation of the biosyngas. Introducing impurity in the syngas flow might affect the catalyst differently than by impregnation as done in this study. Lastly, the minimum tolerance of phosphorous contamination for Fischer-Tropsch catalysts should be identified to determine the amount of impurity in the biosyngas that may be acceptable for use in the Fischer-Tropsch synthesis.

References

[1] A. S. Groven, "Conversion of biomass-derived synthesis gas to hydrocarbons by fischer-tropsch synthesis using cobalt-based catalysts," 2021.

[2] S. Mailaram, P. Kumar, A. Kunamalla, P. Saklecha, and S. K. Maity, *Biomass, biorefinery, and biofuels*. Elsevier, 2021.

[3] P. J. Woolcock and R. C. Brown, "A review of cleaning technologies for biomass-derived syngas," *Biomass and Bioenergy*, vol. 52, pp. 54–84, 5 2013.

[4] H. Kargbo, J. S. Harris, and A. N. Phan, ""drop-in" fuel production from biomass: Critical review on techno-economic feasibility and sustainability," *Renewable and Sustainable Energy Reviews*, vol. 135, p. 110168, 1 2021.

[5] "Net zero by 2050." https://www.iea.org/reports/net-zero-by-2050, 2021.

[6] "Renewable energy." https://www.c2es.org/content/renewable-energy/. Accessed 07.05.2022.

[7] R. C. Baliban, J. A. Elia, and C. A. Floudas, "Biomass to liquid transportation fuels (btl) systems: process synthesis and global optimization framework," *Energy Environ. Sci.*, vol. 6, pp. 267–287, 2013.

[8] S. V. Vassilev, D. Baxter, L. K. Andersen, and C. G. Vassileva, "An overview of the chemical composition of biomass," *Fuel*, vol. 89, pp. 913–933, 5 2010.

[9] A. Lappas and E. Heracleous, *Production of biofuels via Fischer–Tropsch synthesis*. Elsevier, 2016.

[10] R. G. dos Santos and A. C. Alencar, "Biomass-derived syngas production via gasification process and its catalytic conversion into fuels by fischer tropsch synthesis: A review," *International Journal of Hydrogen Energy*, vol. 45, pp. 18114–18132, 7 2020.

[11] E. Østbye Pedersen, I.-H. Svenum, and E. A. Blekkan, "Mn promoted co catalysts for fischer-tropsch production of light olefins – an experimental and theoretical study," *Journal of Catalysis*, vol. 361, 2018.

[12] I. Tiseo, "Ethylene demand and production capacity worldwide from 2015 to 2022." https://www.statista.com/statistics/1246694/ethylene-demand-capacity-forecast-worldwide/, 2021.

[13] I. Amghizar, J. N. Dedeyne, D. J. Brown, G. B. Marin, and K. M. Van Geem, "Sustainable innovations in steam cracking: Co2 neutral olefin production," *React. Chem. Eng.*, vol. 5, pp. 239–257, 2020.

[14] N. U. of Life Sciences (NMBU), "Bio4fuels." https://www.nmbu.no/en/services/centers/bio4fuels. Accessed 09.12.2021.

[15] U. E. I. Administration, "Biomass explained - biomass and the environment," 2020. Accessed 10.12.2021.

[16] S. S. Ail and S. Dasappa, "Biomass to liquid transportation fuel via fischer tropsch synthesis – technology review and current scenario," *Renewable and Sustainable Energy Reviews*, vol. 58, pp. 267–286, 2016.

[17] I. Dimitriou, H. Goldingay, and A. V. Bridgwater, "Techno-economic and uncertainty analysis of biomass to liquid (btl) systems for transport fuel production," *Renewable and Sustainable Energy Reviews*, vol. 88, pp. 160–175, 2018.

[18] M. I. Gonzalez, B. Kraushaar-Czarnetzki, and G. Schaub, "Process comparison of biomass-to-liquid (btl) routes fischer–tropsch synthesis and methanol to gasoline," *Biomass Conversion and Biorefinery*, vol. 1, pp. 229–243, 12 2011.

[19] E. D. Gemechu and A. Kumar, *The environmental performance of hydrogen production pathways based on renewable sources*. Elsevier, 2021.

[20] W. Zhang, "Automotive fuels from biomass via gasification," *Fuel Processing Technology*, vol. 91, pp. 866–876, 2010.

[21] Z. Gholami, N. A. M. Zabidi, F. Gholami, O. B. Ayodele, and M. Vakili, "The influence of catalyst factors for sustainable production of hydrocarbons via fischer-tropsch synthesis," *Reviews in Chemical Engineering*, vol. 33, 2017.

[22] N. Nesterenko, J. Aguilhon, P. Bodart, D. Minoux, and J.-P. Dath, *Methanol to Olefins*. Elsevier, 2016.

[23] T. K. Phung, T. L. M. Pham, K. B. Vu, and G. Busca, "(bio)propylene production processes: A critical review," *Journal of Environmental Chemical Engineering*, vol. 9, p. 105673, 8 2021.

[24] I. Amghizar, L. A. Vandewalle, K. M. V. Geem, and G. B. Marin, "New trends in olefin production," *Engineering*, vol. 3, pp. 171–178, 4 2017.

[25] H. M. T. Galvis and K. P. de Jong, "Catalysts for production of lower olefins from synthesis gas: A review," *ACS Catalysis*, vol. 3, pp. 2130–2149, 9 2013.

[26] J. A. Moulijn, M. Makkee, and A. W. V. Diepen, *Chemical Process Technology*. John Wiley & Sons Ltd, 2 ed., 2013.

[27] M. N. Hassankiadeh, A. Khajehfard, and M. Golmohammadi, "Kinetic and product distribution modeling of fischer-tropsch synthesis in a fluidized bed reactor," *International Journal of Chemical Engineering and Applications*, pp. 400–403, 2012.

[28] A. A. Adesina, "Hydrocarbon synthesis via fischer-tropsch reaction: travails and triumphs," *Applied Catalysis A: General*, vol. 138, pp. 345–367, 1996.

[29] A. de Klerk, *Fischer–Tropsch Synthesis*. Wiley, 2011.

[30] B. Todic, T. Bhatelia, G. F. Froment, W. Ma, G. Jacobs, B. H. Davis, and D. B. Bukur, "Kinetic model of fischer–tropsch synthesis in a slurry reactor on co–re/al ¡sub¿2¡/sub¿ o ¡sub¿3¡/sub¿ catalyst," *Industrial & Engineering Chemistry Research*, vol. 52, pp. 669–679, 2013.

[31] R. C. Brady and R. Pettit, "Mechanism of the fischer-tropsch reaction. the chain propagation step," *Journal of the American Chemical Society*, vol. 103, pp. 1287–1289, 3 1981.

[32] C. Wang and J. Ekerdt, "Evidence for alkyl intermediates during fischer-tropsch synthesis and their relation to hydrocarbon products," *Journal of Catalysis*, vol. 86, pp. 239–244, 4 1984.

[33] M. E. Dry, "The fischer–tropsch process: 1950–2000," *Catalysis Today*, vol. 71, pp. 227–241, 1 2002.

[34] A. B. Fontenelle and F. A. N. Fernandes, "Comprehensive polymerization model for fischer-tropsch synthesis," *Chemical Engineering & Technology*, vol. 34, pp. 963–971, 6 2011.

[35] M. Rønning, "Reaction kinetics and catalysis," 2020. Lecture notes from topics "Fischer-Tropsch synthesis kinetics" and "Catalyst deactivation".

[36] S. Soled, E. Iglesia, and R. A. Fiato, "Activity and selectivity control in iron catalyzed fischer-tropsch synthesis," *Catalysis Letters*, vol. 7, pp. 271–280, 1991.

[37] I. Chorkendorff and J. Niemantsverdriet, *Concepts of Modern Catalysis and Kinetics*. WILET-VCH GmbH & Co. KGaA, 1 ed., 2003.

[38] L. Gavrilović, E. A. Jørgensen, U. Pandey, K. R. Putta, K. R. Rout, E. Rytter, M. Hillestad, and E. A. Blekkan, "Fischer-tropsch synthesis over an alumina-supported cobalt catalyst in a fixed bed reactor – effect of process parameters," *Catalysis Today*, vol. 369, pp. 150–157, 6 2021.

[39] M. E. Dry, "Practical and theoretical aspects of the catalytic fischer-tropsch process," *Applied Catalysis A: General*, vol. 138, pp. 319–344, 5 1996.

[40] A. Lillebø, E. Rytter, E. A. Blekkan, and A. Holmen, "Fischer–tropsch synthesis at high conversions on al2o3 - supported co catalysts with different h2/co levels," *Industrial & Engineering Chemistry Research*, vol. 56, pp. 13281–13286, 11 2017.

[41] D. Tristantini, S. Lögdberg, B. Gevert, Øyvind Borg, and A. Holmen, "The effect of synthesis gas composition on the fischer–tropsch synthesis over co/γ-al2o3 and co–re/γ-al2o3 catalysts," *Fuel Processing Technology*, vol. 88, pp. 643–649, 7 2007.

[42] E. Rytter, N. E. Tsakoumis, and A. Holmen, "On the selectivity to higher hydrocarbons in co-based fischer–tropsch synthesis," *Catalysis Today*, vol. 261, pp. 3–16, 3 2016.

[43] S. Krishnamoorthy, M. Tu, M. P. Ojeda, D. Pinna, and E. Iglesia, "An investigation of the effects of water on rate and selectivity for the fischer–tropsch synthesis on cobalt-based catalysts," *Journal of Catalysis*, vol. 211, pp. 422–433, 10 2002.

[44] S. Storsaeter, O. Borg, E. Blekkan, and A. Holmen, "Study of the effect of water on fischer–tropsch synthesis over supported cobalt catalysts," *Journal of Catalysis*, vol. 231, pp. 405–419, 4 2005.

[45] E. A. Blekkan, Øyvind Borg, V. Frøseth, and A. Holmen, *Fischer-Tropsch synthesis on cobalt catalysts: the effect of water*. Royal Society of Chemistry, 2007.

[46] Øyvind Borg, S. Storsæter, S. Eri, H. Wigum, E. Rytter, and A. Holmen, "The effect of water on the activity and selectivity for γ-alumina supported cobalt fischer–tropsch catalysts with different pore sizes," *Catalysis Letters*, vol. 107, pp. 95–102, 2 2006.

[47] S. Li, S. Krishnamoorthy, A. Li, G. D. Meitzner, and E. Iglesia, "Promoted iron-based catalysts for the fischer–tropsch synthesis: Design, synthesis, site densities, and catalytic properties," *Journal of Catalysis*, vol. 206, pp. 202–217, 3 2002.

[48] M. Dry, *FT catalysts*. Elsevier, 2004.

[49] E. van Steen and M. Claeys, "Fischer-tropsch catalysts for the biomass-to-liquid (btl)-process," *Chemical Engineering & Technology*, vol. 31, pp. 655–666, 2008.

[50] S. Sie and R. Krishna, "Fundamentals and selection of advanced fischer–tropsch reactors," *Applied Catalysis A: General*, vol. 186, pp. 55–70, 10 1999.

[51] J. Horáček, "Fischer–tropsch synthesis, the effect of promoters, catalyst support, and reaction conditions selection," *Monatshefte für Chemie - Chemical Monthly*, vol. 151, pp. 649–675, 2020.

[52] J. Cheng, P. Hu, P. Ellis, S. French, G. Kelly, and C. M. Lok, "A dft study of the transition metal promotion effect on ethylene chemisorption on co(0001)," *Surface Science*, vol. 603, pp. 2752–2758, 9 2009.

[53] A. Dinse, M. Aigner, M. Ulbrich, G. R. Johnson, and A. T. Bell, "Effects of mn promotion on the activity and selectivity of co/sio2 for fischer-tropsch synthesis," *Journal of Catalysis*, vol. 288, pp. 104–114, 4 2012.

[54] K. Shimura, T. Miyazawa, T. Hanaoka, and S. Hirata, "Fischer–tropsch synthesis over alumina supported cobalt catalyst: Effect of promoter addition," *Applied Catalysis A: General*, vol. 494, pp. 1–11, 3 2015.

[55] D. Das, G. Ravichandran, and D. K. Chakrabarty, "Synthesis of light alkenes from syngas on silicalite-1 supported cobalt and cobalt-manganese catalysts," *Applied Catalysis A: General*, vol. 131, pp. 335–345, 10 1995.

[56] D. Das, G. Ravichandran, and D. K. Chakrabarty, "Conversion of syngas to light olefins over silicalite-1 supported iron and cobalt catalysts: Effect of manganese addition," *Catalysis Today*, vol. 36, pp. 285–293, 6 1997.

[57] F. Morales and B. M-Weckhuysen, *Catalysis*. The Royal Society of Chemistry, 2006.

[58] F. Morales, E. Desmit, F. Degroot, T. Visser, and B. Weckhuysen, "Effects of manganese oxide promoter on the co and h2 adsorption properties of titania-supported cobalt fischer–tropsch catalysts," *Journal of Catalysis*, vol. 246, pp. 91–99, 2 2007.

[59] Øyvind Borg, N. Hammer, B. C. Enger, R. Myrstad, O. A. Lindvåg, S. Eri, T. H. Skagseth, and E. Rytter, "Effect of biomass-derived synthesis gas impurity elements on cobalt fischer–tropsch catalyst performance including in situ sulphur and nitrogen addition," *Journal of Catalysis*, vol. 279, pp. 163–173, 4 2011.

[60] A. H. Lillebø, E. Patanou, J. Yang, E. A. Blekkan, and A. Holmen, "The effect of alkali and alkaline earth elements on cobalt based fischer–tropsch catalysts," *Catalysis Today*, vol. 215, pp. 60–66, 10 2013.

[61] Gavrilović, Save, and Blekkan, "The effect of potassium on cobalt-based fischer–tropsch catalysts with different cobalt particle sizes," *Catalysts*, vol. 9, p. 351, 4 2019.

[62] N. E. Tsakoumis, M. Rønning, Øyvind Borg, E. Rytter, and A. Holmen, "Deactivation of cobalt based fischer–tropsch catalysts: A review," *Catalysis Today*, vol. 154, pp. 162–182, 2010.

[63] Y. Dai, Y. Zhao, T. Lin, S. Li, F. Yu, Y. An, X. Wang, K. Xiao, F. Sun, Z. Jiang, Y. Lu, H. Wang, L. Zhong, and Y. Sun, "Particle size effects of cobalt carbide for fischer–tropsch to olefins," *ACS Catalysis*, vol. 9, pp. 798–809, 2 2019.

[64] F. Sun, R. Yang, Z. Xia, Y. Yang, Z. Zhao, S. Gu, D. Wu, Y. Ding, and Z. Jiang, "Effects of cobalt carbide on fischer–tropsch synthesis with mno supported co-based catalysts," *Journal of Energy Chemistry*, vol. 42, pp. 227–232, 3 2020.

[65] P. Hazemann, D. Decottignies, S. Maury, S. Humbert, F. C. Meunier, and Y. Schuurman, "Selectivity loss in fischer-tropsch synthesis: The effect of cobalt carbide formation," *Journal of Catalysis*, vol. 397, pp. 1–12, 5 2021.

[66] E. Rytter and A. Holmen, "Deactivation and regeneration of commercial type fischer-tropsch co-catalysts—a mini-review," *Catalysts*, vol. 5, pp. 478–499, 3 2015.

[67] P. Munnik, P. E. de Jongh, and K. P. de Jong, "Recent developments in the synthesis of supported catalysts," *Chemical Reviews*, vol. 115, pp. 6687–6718, 7 2015.

[68] A. V. Neimark, L. I. Kheifets, and V. B. Fenelonov, "Theory of preparation of supported catalysts," *Industrial & Engineering Chemistry Product Research and Development*, vol. 20, 1981.

[69] O. Deutschmann, H. Knözinger, K. Kochloefl, and T. Turek, *Heterogeneous Catalysis and Solid Catalysts, 2. Development and Types of Solid Catalysts.* Wiley-VCH Verlag GmbH & Co. KGaA, 2011.

[70] S. Brunauer, P. H. Emmett, and E. Teller, "Adsorption of gases in multimolecular layers," *Journal of the American Chemical Society*, vol. 60, 1938.

[71] E. P. Barrett, L. G. Joyner, and P. P. Halenda, "The determination of pore volume and area distributions in porous substances. i. computations from nitrogen isotherms," *Journal of the American Chemical Society*, vol. 73, 1951.

[72] P. A. Webb, "Introduction to chemical adsorption analytical techniques and their applications to catalysis." https://www.micromeritics.com/Repository/Files/intro_to_chemical_adsorption_techniques_catalysis.pdf, 2003.

[73] "What is tpr?." https://www.hidenanalytical.com/blog/what-is-tpr/, 2018. Accessed 04.04.2022.

[74] N. W. Hurst, S. J. Gentry, A. Jones, and B. D. McNicol, "Temperature programmed reduction," *Catalysis Reviews*, vol. 24, pp. 233–309, 1982.

[75] H.-M. Koo, B. S. Lee, M.-J. Park, D. J. Moon, H.-S. Roh, and J. W. Bae, "Fischer–tropsch synthesis on cobalt/al2o3-modified sic catalysts: effect of cobalt–alumina interactions," *Catal. Sci. Technol.*, vol. 4, pp. 343–351, 2014.

[76] A. Lapidus, A. Krylova, V. Kazanskii, V. Borovkov, A. Zaitsev, J. Rathousky, A. Zukal, and M. Janc ˇálková, "Hydrocarbon synthesis from carbon monoxide and hydrogen on impregnated cobalt catalysts part i. physico-chemical properties of 10% cobalt/alumina and 10% cobalt/silica," *Applied Catalysis*, vol. 73, pp. 65–81, 5 1991.

[77] G. Jacobs, T. K. Das, Y. Zhang, J. Li, G. Racoillet, and B. H. Davis, "Fischer–tropsch synthesis: support, loading, and promoter effects on the reducibility of cobalt catalysts," *Applied Catalysis A: General*, vol. 233, pp. 263–281, 7 2002.

[78] F. Morales, F. deGroot, O. Gijzemann, A. Mens, O. Stephan, and B. Weckhuysen, "Mn promotion effects in co/tio2 fischer-tropsch catalysts as investigated by xps and stem-eels," *Journal of Catalysis*, vol. 230, pp. 301–308, 3 2005.

[79] F. Morales, D. Grandjean, A. Mens, F. M. F. de Groot, and B. M. Weckhuysen, "X-ray absorption spectroscopy of mn/co/tio2 fischer-tropsch catalysts: Relationships between preparation method, molecular structure, and catalyst performance," *The Journal of Physical Chemistry B*, vol. 110, pp. 8626–8639, 5 2006.

[80] Øyvind Borg, V. Frøseth, S. Storsæter, E. Rytter, and A. Holmen, *Fischer-tropsch synthesis. recent studies on the relation between the properties of supported cobalt catalysts and the activity and selectivity.* Elsevier, 2007.

[81] E. Iglesia, S. L. Soled, and R. A. Fiato, "Fischer-tropsch synthesis on cobalt and ruthenium. metal dispersion and support effects on reaction rate and selectivity," *Journal of Catalysis*, vol. 137, pp. 212–224, 9 1992.

[82] J. Hong, B. Wang, G. Xiao, N. Wang, Y. Zhang, A. Y. Khodakov, and J. Li, "Tuning the metal-support interaction and enhancing the stability of titania-supported cobalt fischer-tropsch catalysts via carbon nitride coating," *ACS Catalysis*, vol. 10, pp. 5554–5566, 5 2020.

[83] Øyvind Borg, M. Rønning, S. Storsæter, W. van Beek, and A. Holmen, *Identification of Cobalt Species During Temperature Programmed Reduction of Fischer-Tropsch Catalysts.* Elsevier, 2007.

[84] G. R. Johnson, S. Werner, and A. T. Bell, "An investigation into the effects of mn promotion on the activity and selectivity of co/sio2 for fischer-tropsch synthesis: Evidence for enhanced co adsorption and dissociation," *ACS Catalysis*, vol. 5, pp. 5888–5903, 10 2015.

[85] G. R. Johnson and A. T. Bell, "Effects of lewis acidity of metal oxide promoters on the activity and selectivity of co-based fischer–tropsch synthesis catalysts," *Journal of Catalysis*, vol. 338, pp. 250–264, 6 2016.

[86] M. Martinelli, M. K. Gnanamani, S. D. Hopps, D. E. Sparks, A. MacLennan, Y. Hu, B. H. Davis, and G. Jacobs, "Effect of phosphorus on the activity and stability of supported cobalt catalysts for fischer-tropsch synthesis," *ChemCatChem*, vol. 10, pp. 3709–3716, 9 2018.

Appendix

A Catalyst Synthesis Calculations

The molar masses of all components needed in the catalyst synthesis are given in Table A.1.

Table A.1: Molar masses of components used for calculations of the catalyst synthesis.

Component	**Molar mass [g/mol]**
H_2O	18.015
Co	58.93
Mn	54.94
Re	186.207
P	30.97
$Co(NO_2)_2{\cdot}6H_2O$	291.03
$Mn(NO_3)_2{\cdot}4H_2O$	251.01
$HReO_4$	251.206
H_2PO_4	85
MnO_2	86.94
Co_3O_4	240.8
ReO_2	218.21
P_2O_{10}	283.88

As most components will be present in its oxidized state during the impregnation, a factor taking that in consideration for the molar masses were calculated for all relevant elements. These factors (Table A.2) were found be dividing the molar masses of the metal oxide and corresponding metal. An example for cobalt is given in Equation A.1, where F denotes the molar mass factor and M represents the molar mass.

$$F_{Co_3O_4} = \frac{M_{Co_3O_4}}{3 \cdot M_{Co}} = \frac{240.8}{3 \cdot 58.93} = 1.362 \tag{A.1}$$

Table A.2: Calculated factors for molar masses taking in consideration that the metals are present in its oxidized state during catalyst synthesis.

Oxide	**Factor**
MnO_2	1.582
Co_3O_4	1.362
ReO_2	1.172
P_2O_{10}	2.292

Additional information needed for the calculations is the pore volume of the support materials and the desired element distribution. The pore volume for γ-Al_2O_3 was 0.7cm^3/g, while SiO_2#1 had a pore volume of 1.5 cm^3/g, and the pore volume of SiO_2#2 was 0.9cm^3/g. The desired element distribution of the catalysts are given in Table A.3.

Table A.3: The element distribution for calculations of the catalyst synthesis showing the amounts of cobalt, rhenium, manganese and phosphorous for the different catalysts.

Catalyst	**Co [wt%]**	**Re [wt%]**	**Mn [wt%]**	**P [wt%]**
Reference catalysts	15	0.5	-	-
Standard catalysts	15	0.5	3.75	-
1.5%Mn catalyst	15	0.5	1.5	-
5%Mn catalyst	15	0.5	5	-
P1 catalysts	15	0.5	3.75	0.17
P2 catalysts	15	0.5	3.75	0.67

As described in the methods for catalyst impregnation, manganese was the first component to be impregnated for the catalysts containing manganese. The acquired amount of Mn was calculated as shown in Equation A.2, where m represents the mass in grams, and *sup.* represents the support material. The amount of support material was known.

$$m_{Mn} = \frac{\%_{Mn} \cdot m_{sup.}}{(1 - \%_{Mn}) \cdot F_{\mathrm{MnO_2}}} \tag{A.2}$$

When the mass of required Mn was known, the acquired amount of manganese precursor was calculated accordingly:

$$m_{Mn(\mathrm{NO_3})_2 4\mathrm{H_2O}} = \frac{m_{Mn} \cdot M_{Mn(\mathrm{NO_3})_2 4\mathrm{H_2O}}}{M_{Mn}} \tag{A.3}$$

Finally, the amount of DI water acquired for reaching the liquid absorption capacity was found by Equation A.4, taking into consideration the water contribution from the precursor ($\mathrm{l_{H_2O}}_{prec.}$). l represents the liquid amount in ml and V_{pore} is the pore volume capacity of the support material (cm^3/g).

$$l_{DI} = m_{sup.} \cdot V_{pore} - l_{\mathrm{H_2O prec}}. \tag{A.4}$$

Impregnation of cobalt was calculated in the same matter as manganese, while the amount of rhenium was added to the impregnation solution before adding all of the DI water. It was assumed that the previous impregnation of manganese had a negligible change on the absorption capacity of the support material. The amount of Re and precursor ($HReO_4$) in grams was calculated in the same way as in Equation A.2 and Equation A.3. The calculated amount of precursor ($HReO_4$) was converted to liquid amounts in ml by dividing with its density (2.16 g/ml).

The assumption of negligible change in liquid absorption capacity after the second impregnation was also made for the addition of phosphorous. The acquired amount of phosphorous precursor was

found in the same way as described for rhenium. The amount of DI water required for the impregnation was found by multiplying the amount of support (in this case the catalyst $CoReMn/SiO_2$) with the pore volume of the support and subtracting the amount of precursor.

B Additional Results

Isotherms from H_2-chemisorption for the P2-CoReMn/SiO_2#2 and CoReMn/Al_2O_3 catalysts are shown in Figure B.1 and Figure B.2, respectively. The alumina-supported catalyst display a normal Langmuir isotherm, as opposed to the P2 catalyst.

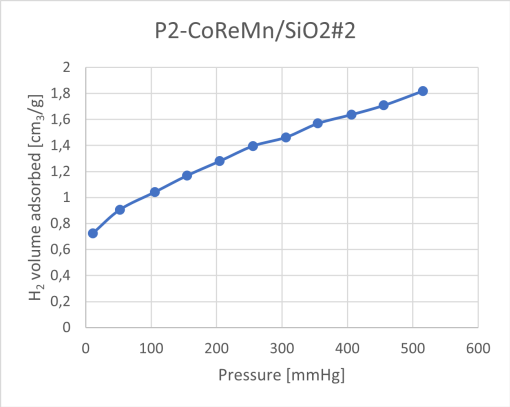

Figure B.1: The adsorption isotherm of catalyst P2-CoReMn/SiO_2#2 obtained from H_2-chemisorption. The isotherm dos not behave as a normal Langmuir isotherm.

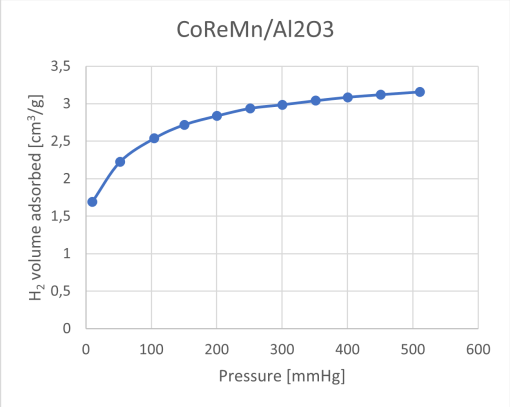

Figure B.2: The adsorption isotherm of catalyst CoReMn/Al_2O_3 from obtained from H_2-chemisorption. The isotherm behaves as a Langmuir isotherm.

The XRD-patterns for the catalysts containing phosphorous are displayed below. Figure B.3 show the catalysts with silica#1 as support material, and Figure B.4 show the catalysts with silica#2 as support material. The catalysts with phosphorous are compared to its corresponding standard catalyst. No differences in XRD-patterns are observed after P-impregnation.

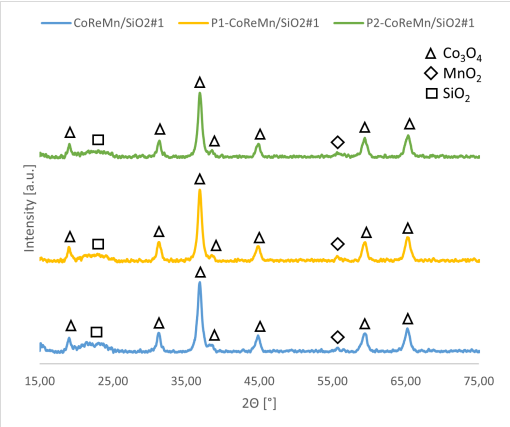

Figure B.3: XRD patterns for the standard SiO_2#1 supported catalyst compared to the catalysts with 1700 (P1) and 6700 ppmw (P2) phosphorous contamination.

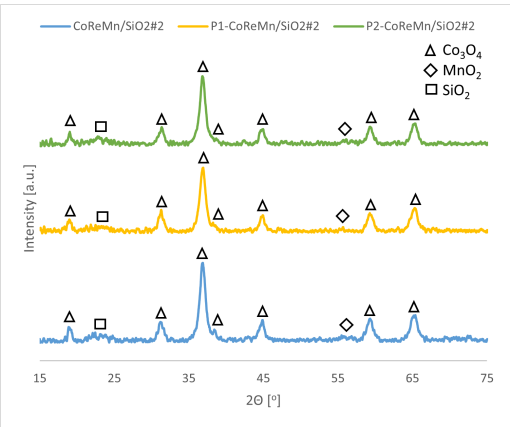

Figure B.4: XRD patterns for the standard SiO_2#2 supported catalyst compared to the catalysts with 1700 (P1) and 6700 ppmw (P2) phosphorous contamination.

C Risk Assessment

Detailed Risk Report

ID	43416	**Status**	**Date**
Risk Area	Risikovurdering: Helse, miljø og sikkerhet (HMS)	Created	27.08.2021
Created by	Anette Synnøve Groven	Assessment started	27.08.2021
Responsible	Anette Synnøve Groven	Measures decided	
		Closed	

Risk Assessment:

CAT, Master Student, 2022, Anette Groven

Valid from-to date:
8/27/2021 - 8/27/2024

Location:
IKP, K5, Chemistryhall D; rig 1.4

Goal / purpose
Risk assessment for my work as a Master student on biofuel production from biomass by Fischer Tropsh. Flow sheet of the rig is in the attachments.

Background
Catalyst preparation.
Chemicals:
- Cobalt(II) nitrate hexahydrate (precursor)
- Alumina Sasol Puralox SCCa (Particle size = 60-150µm)
Methods:
- Evaporation-drying (85-120ºC)
- Calcination (700-1000ºC)

Cobalt impregnation with water.
Chemicals:
- Co(NO3)2·6 H2O
Methods:
- Co(NO3)2·6 H2O dissolved in distilled water and stirred for 2h at room temperature.
- Addition of support powder while strirring for 18h at room temperature.
- Mixture evaporated at 358K for 2 days.
- Solid dried at 373K overnight.
- Calcination (500-800ºC) of the solid for 5h (3K/min).

Characterization Techniqes
- BET using nitrogen/N2 adsorption-desorption
- XRF
- XRD
- Chemisorption using hydrogen
- TPR
- TGA

Set up of Fischer Tropsch rig
Gases being used are CO and H2. It is important to be careful, ask for help if necessary.
Leak test with detector must be preformed. After mounting reactor it is pressurized with He and leak-tested before any CO or H2 is used.
Waxes and lighter hydrocarbons (ish C6) are collected in two separate pots, which needs to be emptied every now and then. Wear face-protection and heat resistant gloves when doing this.

Description and limitations

Personal protective equipment.
Read SDS (If you see healthsentences H340, H350 and H350i you could register in Eco Exposure)
Proper training
Safety measures
Be aware of physical risks such as pressure and temperature etc.

Prerequesites, assumptions and simplifications

Will use the IKP lab activity group in Microsoft Teams to register my lab prenece in Hall D.
Will keep 1 meter distance to other people, and if this is not possible I will wear a mask.
Download sds (safety data sheets) for chemicals and gases.
Refer to completed risk assesment.

Switch off procedure for BET set up:
- Stop the analysis in the computer.
- Remove the tube sample from the unit.
- Insert the metal rod in the unit.

Switch off procedure for chemisorption set up:
- Close all valves in the software.
- Open valve 9, C6, CS, 7 and 5 to flow He into the system.
- When the pressure is around 700mmHg close alle valves.
- Open the reactor and remove the tube sample.

Risk related the shortage of presonnel in the labs:
- Plan eerything in advantage and communicate the plan to the engineers.
- Take extra care in the leak test before running any reaction.
- Not running reactions after 4PM.

Safety measures related to spread of covid19 infections:
- Keep 1 meter distance to other people. If this is not possible, wear a mask.
- Disinfect all contact surfaces with ethanol before and after use.
- Wash hands as often as possible
- Use nitrile gloves when touching shared lab set-ups and equpment
- Update the excel sheet in the IKP Lab activity gruop in Microsoft Teams about weekly planning a week in advance.

Attachments

CO_SDS.pdf
ReSDS.pdf
H2_SDS.pdf
FT-flowsheet.PNG
PSDS.pdf
CobaltNitrateHex_SDS.pdf
ManganeseNitrateSDS.pdf
Unit_card_rig1.4.docx
MSDS Silica Dioxide.pdf

References

[Ingen registreringer]

Summary, result and final evaluation

The summary presents an overview of hazards and incidents, in addtition to risk result for each consequence area.

Hazard:	**Handling toxic (CO)/inflammable gases (H2)**			
Incident:	**Danger of explosion**			
Consequence area:	Helse	Risk before measures:	Risiko after measures:	
	Materielle verdier	Risk before measures:	Risiko after measures:	
Incident:	**Danger of poisoning**			
Consequence area:	Helse	Risk before measures:	Risiko after measures:	
	Ytre miljø	Risk before measures:	Risiko after measures:	
Hazard:	**Pressurize and high temperature installation**			
Incident:	**Danger of explosion**			
Consequence area:	Helse	Risk before measures:	Risiko after measures:	
	Materielle verdier	Risk before measures:	Risiko after measures:	
Incident:	**Burn damage**			
Consequence area:	Helse	Risk before measures:	Risiko after measures:	
	Materielle verdier	Risk before measures:	Risiko after measures:	
Hazard:	**Hot products**			
Incident:	**Burn damage**			
Consequence area:	Helse	Risk before measures:	Risiko after measures:	

Hazard:	**Handling Chemicals (Co(NO3)2·6H2O)**				
Incident:	**Danger of contact with skin or inhalation. Spilling Cobalt(II) nitrate hexahydrate.**				
Consequence area:	Helse	Risk before measures:	Risiko after measures:		
	Ytre miljø	Risk before measures:	Risiko after measures:		
Incident:	**Danger of burning and inhale vapors. Heating/Evaporating samples.**				
Consequence area:	Helse	Risk before measures:	Risiko after measures:		
	Ytre miljø	Risk before measures:	Risiko after measures:		
Hazard:	**N2-Adsorption/Desorption**				
Incident:	**Burn damage. Handling Liquid N2.**				
Consequence area:	Helse	Risk before measures:	Risiko after measures:		
	Materielle verdier	Risk before measures:	Risiko after measures:		

Final evaluation

Organizational units and people involved

A risk assessment may apply to one or more organizational units, and involve several people. These are lsited below.

Organizational units which this risk assessment applies to

- Institutt for kjemisk prosessteknologi

Participants

Oscar Luis Ivanez Encinas
Edd Anders Blekkan
Estelle Marie M. Vanhaecke

Readers

[Ingen registreringer]

Others involved/stakeholders

[Ingen registreringer]

The following accept criteria have been decided for the risk area Risikovurdering: Helse, miljø og sikkerhet (HMS):

Helse	Materielle verdier	Omdømme	Ytre miljø
			

Overview of existing relevant measures which have been taken into account

The table below presents existing measures which have been take into account when assessing the likelihood and consequence of relevant incidents.

Hazard	Incident	Measures taken into account
Handling toxic (CO)/inflammable gases (H2)	Danger of explosion	Gas detection
	Danger of explosion	Local exhaust
	Danger of explosion	Security data sheet
	Danger of explosion	Safety Equipment
	Danger of poisoning	Gas detection
	Danger of poisoning	Local exhaust
	Danger of poisoning	Security data sheet
	Danger of poisoning	Safety Equipment
Pressurize and high temperature installation	Danger of explosion	Gas detection
	Danger of explosion	Local exhaust
	Danger of explosion	Security data sheet
	Danger of explosion	Safety Equipment
	Burn damage	Gas detection
	Burn damage	Local exhaust
	Burn damage	Security data sheet
	Burn damage	Safety Equipment
Hot products	Burn damage	Instrument/Method training
	Burn damage	Safety Equipment
	Burn damage	Apparatur card
Handling Chemicals (Co(NO3)2·6H2O)	Danger of contact with skin or inhalation. Spilling Cobalt(II) nitrate hexahydrate.	Gas detection
	Danger of contact with skin or inhalation. Spilling Cobalt(II) nitrate hexahydrate.	Local exhaust
	Danger of contact with skin or inhalation. Spilling Cobalt(II) nitrate hexahydrate.	Security data sheet
	Danger of contact with skin or inhalation. Spilling Cobalt(II) nitrate hexahydrate.	Safety Equipment
	Danger of burning and inhale vapors. Heating/Evaporating samples.	Instrument/Method training
	Danger of burning and inhale vapors. Heating/Evaporating samples.	Local exhaust
	Danger of burning and inhale vapors. Heating/Evaporating samples.	Safety Equipment
N2-Adsorption/Desorption	Burn damage. Handling Liquid N2.	Instrument/Method training
	Burn damage. Handling Liquid N2.	Safety Equipment

Existing relevant measures with descriptions:

Gas detection

Know where the gas detectors are installed. Use portable detectors if not installed.
Verify that the gas detector is working before experiments.
Understand the different alarms and how to act with each one.

Instrument/Method training

Understand the procedure of techniques and equipment in the training.
Ask about any possible troubles and risks and doubts about the procedure.
Read and familiarize with the procedure before experiments.

Local exhaust

Verify that the local exhaust is working properly before experiments.

Security data sheet

Read and familiarize with the precautions and actions required with the risk associated with the chemicals.

Safety Equipment

Safety goggles mandatory in all laboratories
Lab coat
Gloves (read sds in order to choose the correct gloves)
Gas mask (read sds in order to choose the correct filters)
Filter mask (read sds in order to choose the correct type)
Noise protector (headphones)
Protection helmet

Leak test

Verify the isolation of the installation before running experiments.

Apparatur card

Learn and understand the risks associated with the installation, the gasses used, the operationn temperature and how to act in case of emergency.

General requirements due to Covid19

The number of people who work in laboratories must be reduced to an absolute minimum, while avoiding solitary work.
Existing measures for laboratories, such as requirements for using personal protective equipment and fume cupboards, must be followed.
Thorough hand washing, or hand desinfaction if necessary, must be completed before waste bags or bins are handled.
Instruments and equipment must be cleaned before they are taken out of the laboratory.

Protective equipment due to Covid19

Personal protective equipment must only be used by 1 person.
Protective equipment that will be used several times must as far as possible be cleaned/disinfected after use and stored in an airtight box/bag when it is in use.
If protective equipment must be used by several people, it must always be thoroughly cleaned/derinfected before and after use.
If personal protective equipment is not available: A risk assessment must be done to identify which tasks can still be performed.

Cleaning rules due to Covid19

Regular cleaning must be done in accordance with the agreement between the unit and Campus Services Division.
The user must ensure cleaning and, where applicable, disinfection of equipment (Keyboard, mouse, desk , door knob and card reader), especially equipment that is used by more than one person, surfaces, and touch points, immediately after completing the work.
The general rule is that cleaning agents and water must be applies with a cloth, preferable a disposable cloth.
Disinfactants can then be applied as needed.
Remove unnecessary papers, books and other items from worktops and tables.

Risk analysis with evaluation of likelihood and consequence

This part of the report presents detailed documentation of hazards, incidents and causes which have been evaluated. A summary of hazards and associated incidents is listed at the beginning.

The following hazards and incidents has been evaluated in this risk assessment:

- **Handling toxic (CO)/inflammable gases (H2)**
  - Danger of explosion
  - Danger of poisoning
- **Pressurize and high temperature installation**
  - Danger of explosion
  - Burn damage
- **Hot products**
  - Burn damage
- **Handling Chemicals (Co(NO3)2·6H2O)**
  - Danger of contact with skin or inhalation. Spilling Cobalt(II) nitrate hexahydrate.
  - Danger of burning and inhale vapors. Heating/Evaporating samples.
- **N2-Adsorption/Desorption**
  - Burn damage. Handling Liquid N2.

Detailed view of hazards and incidents:

Hazard: Handling toxic (CO)/inflammable gases (H2)

Incident: Danger of explosion

Likelihood of the incident (common to all consequence areas): **Less likely (2)**

Kommentar:

Use of local exhaust.
Gas detector.
Local alarm.
Leak test.
After mounting reactor it is pressureized with He and leak-tested before CO or H2 is used.

Consequence area: Helse

Risk:

Assessed consequence: **Very large (4)**

Comment: CO
H220 - EXTREMELY FLAMMABLE GAS
H280 - CONTAINS GAS UNDER PRESSURE; MAY EXPLODE IF HEATED
H331 - TOXIC I INHALED
H360 - MAY DAMAGE FERTILITY OR THE UNBORN CHILD
H372 - CAUSES DAMAGE TO ORGANS (CENTERAL NERSVOUS SYSTEM) THROUGH PROLONGED OR REPEATED EXPOSURE
CGA-HG04 - MAY FORM EXPLOSIVE MIXTURES WITH AIR

H2
H220 - EXTREMELY FLAMMABLE GAS
H280 - CONTAINS GAS UNDER PRESSURE; MAY EXPLODE IF HEATED
MAY DISPLACE OXYGEN AND CAUSE RAPID SUFFOCATION

Consequence area: Materielle verdier

Risk:

Assessed consequence: **Large (3)**

Comment: CO
H220 - EXTREMELY FLAMMABLE GAS
H280 - CONTAINS GAS UNDER PRESSURE; MAY EXPLODE IF HEATED
H331 - TOXIC IF INHALED

H2
H220 - EXTREMELY FLAMMABLE GAS
H280 - CONTAINS GAS UNDER PRESSURE; MAY EXPLODE IF HEATED
MAY FORM EXPLOSIVE MIXTURES WITH AIR

Incident: Danger of poisoning

Likelihood of the incident (common to all consequence areas): **Unlikely (1)**

Kommentar:

Use of local exhaust.
Gas detector.
Local alarm.
Leak test.
After mounting reactor it is pressurized with He and leak-tested before any CO or H2 is used.

Consequence area: Helse

Risk:

Assessed consequence: **Catastrophical (5)**

Comment: CO
H220 - EXTREMELY FLAMMABLE GAS
H280 - CONTAINS GAS UNDER PRESSURE; MAY EXPLODE IF HEATED
H331 - TOXIC I INHALED
H360 - MAY DAMAGE FERTILITY OR THE UNBORN CHILD
H372 - CAUSES DAMAGE TO ORGANS (CENTERAL NERSVOUS SYSTEM) THROUGH PROLONGED OR REPEATED EXPOSURE
CGA-HG04 - MAY FORM EXPLOSIVE MIXTURES WITH AIR
CHA-HG10 - ASPHYXIATING EVEN WITH ADEQUATE OXYGEN

H2
H220 - EXTREMELY FLAMMABLE GAS
H280 - CONTAINS GAS UNDER PRESSURE; MAY EXPLODE IF HEATED
MAY DISPLACE OXYGEN AND CAUSE RAPID SUFFOCATION

Consequence area: Ytre miljø

Risk:

Assessed consequence: **Large (3)**

Comment: CO
H220 - EXTREMELY FLAMMABLE GAS
H280 - CONTAINS GAS UNDER PRESSURE; MAY EXPLODE IF HEATED
H331 - TOXIC I INHALED

H2
H220 - EXTREMELY FLAMMABLE GAS
H280 - CONTAINS GAS UNDER PRESSURE; MAY EXPLODE IF HEATED

Hazard: Pressurize and high temperature installation

Incident: Danger of explosion

Likelihood of the incident (common to all consequence areas): **Less likely (2)**

Kommentar:

Use of local exhaust.
Gas detector.
Local alarm.
Leak test.
Rig training.
After mounting reactor it is pressurized with He and leak-tested before any CO or H2 is used.

Consequence area: Helse

Risk:

Assessed consequence: **Very large (4)**

Comment: CO
H220 - EXTREMELY FLAMMABLE GAS
H280 - CONTAINS GAS UNDER PRESSURE; MAY EXPLODE IF HEATED
H331 - TOXIC I INHALED
H360 - MAY DAMAGE FERTILITY OR THE UNBORN CHILD
H372 - CAUSES DAMAGE TO ORGANS (CENTERAL NERSVOUS SYSTEM) THROUGH PROLONGED OR REPEATED EXPOSURE
CGA-HG04 - MAY FORM EXPLOSIVE MIXTURES WITH AIR

H2
H220 - EXTREMELY FLAMMABLE GAS
H280 - CONTAINS GAS UNDER PRESSURE; MAY EXPLODE IF HEATED
MAY DISPLACE EXYGEN AND CAUSE RAPID SUFFOCATION

Consequence area: Materielle verdier

Risk:

Assessed consequence: **Large (3)**

Comment: H220 - EXTREMELY FLAMMABLE GAS
H280 - CONTAINS GAS UNDER PRESSURE; MAY EXPLODE IF HEATED
H331 - TOXIC IF INHALED

Incident: Burn damage

Likelihood of the incident (common to all consequence areas): **Unlikely (1)**

Kommentar:

Protective equipment.
Rig training.
After mounting reactor it is pressurized with He and leak-tested before any CO or H2 is used.

Consequence area: Helse

Risk:

Assessed consequence: **Large (3)**

Comment: Operating temperature of 250ºC.

Consequence area: Materielle verdier

Risk:

Assessed consequence: **Medium (2)**

Comment: Bruken equipment.

Hazard: Hot products

Incident: Burn damage

Likelihood of the incident (common to all consequence areas): **Less likely (2)**

Kommentar:

Protective equipment.
Rig training.
Wear face-protection and heat resistant gloves.

Consequence area: Helse

Risk:

Assessed consequence: **Medium (2)**

Comment: Products at high temperature may cause burn damage.

Hazard: Handling Chemicals ($Co(NO_3)_2 \cdot 6H_2O$)

Incident: Danger of contact with skin or inhalation. Spilling Cobalt(II) nitrate hexahydrate.

Likelihood of the incident (common to all consequence areas): **Less likely (2)**

Kommentar:

P280 - Wear protective gloves/ protective clothing/ eye protection/ face protection
P210 - Keep away from heat/sparks/open flames/hot surfaces. - No smoking
P302 + P352 - IF ON SKIN: Wash with plenty of soap and water
P305 + P351 + P338 - IF IN EYES: Rinse cautiously with water for several minutes. Remove contact lenses, if present and
easy to do. Continue rinsing
P310 - Immediately call a POISON CENTER or doctor/ physician

Consequence area: Helse

Risk:

Assessed consequence: **Very large (4)**

Comment: H302 - Harmful if swallowed
H332 - Harmful if inhaled
H317 - May cause an allergic skin reaction
H318 - Causes serious eye damage
H334 - May cause allergy or asthma symptoms or breathing difficulties if inhaled
H341 - Suspected of causing genetic defects
H350i - May cause cancer by inhalation
H360F - May damage fertility

Consequence area: Ytre miljø

Risk:

Assessed consequence: **Very large (4)**

Comment: H410 - Very toxic to aquatic life with long lasting effects

Incident: Danger of burning and inhale vapors. Heating/Evaporating samples.

Likelihood of the incident (common to all consequence areas): **Unlikely (1)**

Kommentar:

Work in fume hood or under local exhaust.
P280 Wear protective gloves/eye protection/face protection.
Use safety equipment.
Wait for cooling down to move the mixture.

Consequence area: Helse

Risk:

Assessed consequence: **Large (3)**

Comment: H332 - Harmful if inhaled
H334 - May cause allergy or asthma symptoms or breathing difficulties if inhaled
H341 - Suspected of causing genetic defects
H350i - May cause cancer by inhalation
H360F - May damage fertility

High temperatures of samples may cause brun damages.

Consequence area: Ytre miljø

Risk:

Assessed consequence: **Small (1)**

Comment: Vapor phase not as dangerous for environment/aquatic life.

Hazard: N2-Adsorption/Desorption

Incident: Burn damage. Handling Liquid N2.

Likelihood of the incident (common to all consequence areas): **Less likely (2)**

Kommentar:

Use of safety equipment.
Wear face-protection and resistant gloves.

Consequence area: Helse

Risk:

Assessed consequence: **Large (3)**

Comment: Liquid nitrogen at 77K will burn the skin on contact.

Consequence area: Materielle verdier

Risk:

Assessed consequence: **Small (1)**

Comment: [Ingen registreringer]

Overview of risk mitiating measures which have been decided:

Below is an overview of risk mitigating measures, which are intended to contribute towards minimizing the likelihood and/or consequence of incidents:

Overview of risk mitigating measures which have been decided, with description:

Detailed view of assessed risk for each hazard/incident before and after mitigating measures

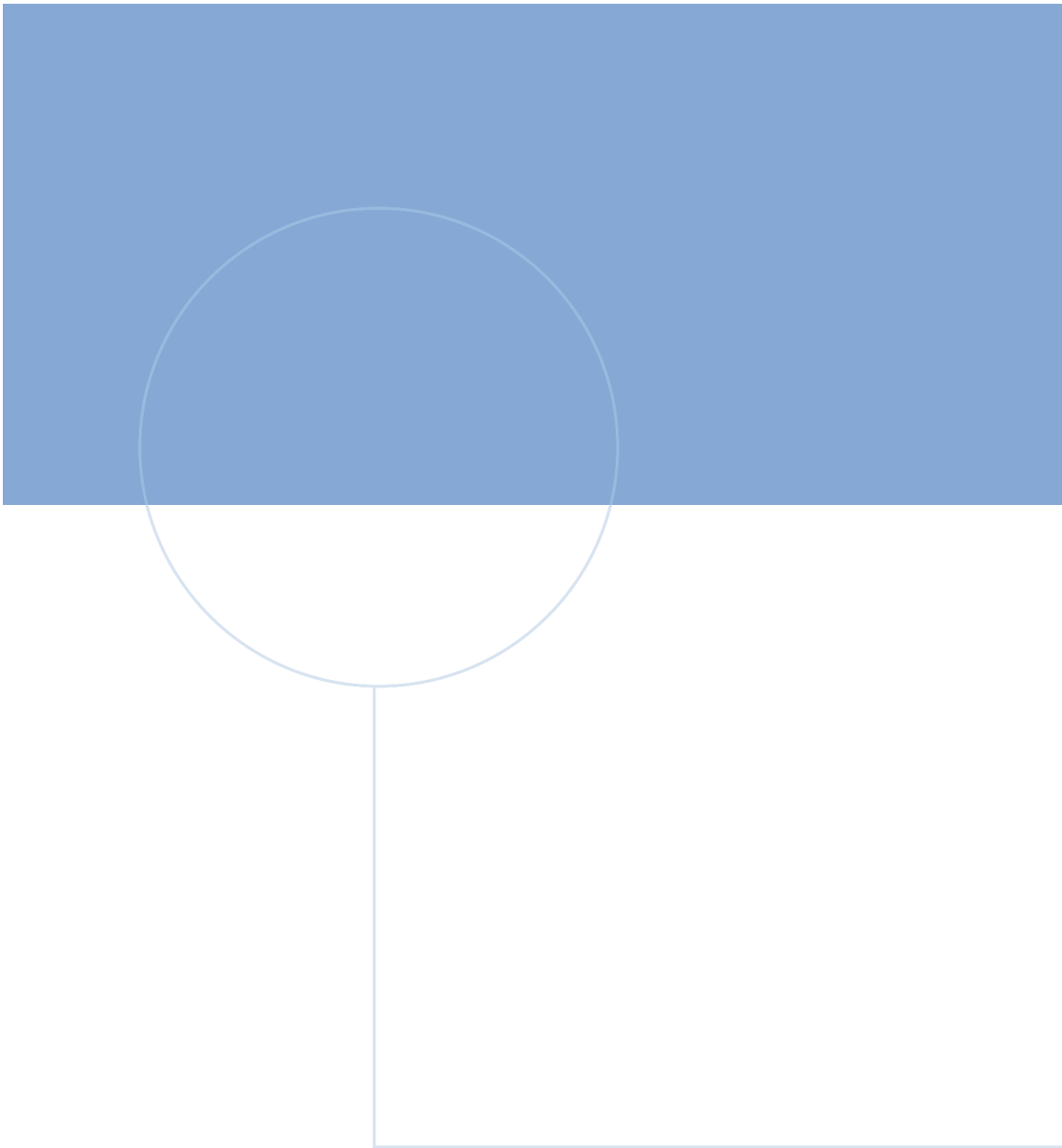

NTNU

Norwegian University of
Science and Technology